

Standard Model anomalies and vacuum stability for lepton portals with extra $U(1)$ symmetry

Carlo Branchina^{‡,1,2}, Hyun Min Lee^{†,2} and Kimiko Yamashita^{*,3}

¹*Department of Physics, University of Calabria, I-87036
Arcavacata di Rende, Cosenza, Italy,
INFN-Cosenza, I-87036 Arcavacata di Rende, Cosenza, Italy.*

²*Department of Physics, Chung-Ang University, Seoul 06974, Korea.*

³*Department of Physics, Ibaraki University, Mito 310-8512, Japan.*

Abstract

Recently, the experimental values of the muon $(g-2)_\mu$ and of the W boson mass m_W have both indicated significant deviations from the SM predictions, motivating the exploration of extensions with extra particles and symmetries. We revisit a lepton portal model with $U(1)'$ gauge symmetry where an extra Higgs doublet, a scalar singlet and one $SU(2)_L$ singlet vector-like fermion are introduced. In this model, $(g-2)_\mu$ can be explained by extra one-loop contributions from the vector-like lepton and the Z' boson, whereas m_W can be increased by a tree-level mixing between the Z and Z' . Setting the Z' and lepton couplings at low energies to account for the SM anomalies, we perform a Renormalization Group analysis to investigate on the high-energy behaviour of the model, in particular on the issue of vacuum stability. We find that in the alignment limit for the two Higgs doublets, the Landau pole and the scale where perturbativity is lost are of order $10 - 100$ TeV, not far from the scales experimentally reached so far, and sensibly lower than the stability scale. We show how the Landau pole can be increased up to $\sim 10^9$ GeV in a misaligned scenario where the experimental anomalies are still accommodated and a positive shift of the Higgs quartic coupling to improve stability can be achieved.

[‡]Email: carlo.branchina@unical.it

[†]Email: hminlee@cau.ac.kr

^{*}Email: kimiko.yamashita.nd93@vc.ibaraki.ac.jp

Contents

1	Introduction	2
2	The model	3
3	Phenomenological constraints on Z'	5
3.1	SM anomalies: muon $g - 2$ and W boson mass	5
3.2	Z' signatures at the LHC	7
4	SM anomalies and running couplings	9
4.1	Tree-level stability of the potential	9
4.2	One-loop effective potential	11
4.3	Conditions from SM anomalies	13
4.4	Running couplings from the alignment limit in the IR	15
4.5	Z' mass dependence of the Landau pole	18
5	General alignment limits in the IR	21
5.1	Detuning quartic couplings	22
5.2	General decoupling of the singlet scalar	25
5.3	Breaking the alignment	27
6	Conclusions	31
A	Mass matrices	32
A.1	Scalar masses	32
A.2	Gauge masses	34
A.3	Fermion masses	35
B	Renormalization Group Equations	35
B.1	Extraction of the scalar RGEs from the potential	35
B.2	Gauge RGEs	37
B.3	Fermion RGEs	37
	References	38

1 Introduction

The measurements of the mass and couplings of the Higgs boson have turned out to be consistent with the Standard Model (SM) predictions. Using the well-known SM relations, we can infer the Higgs quartic coupling λ from the measured Higgs mass m_H at low energy, and extrapolate it to higher energies through Renormalization Group (RG) equations. It has been shown that, within the SM, the running coupling $\lambda(\mu)$ turns negative at high energies due to the large top Yukawa coupling [1], opening the possibility for a decay of the electroweak (EW) vacuum towards the true, deeper vacuum. This is at the origin of the vacuum stability problem in the SM, that might indicate the necessity for threshold corrections from new physics to appear below the stability scale [2], i.e. the scale where $\lambda(\mu)$ turns negative. Therefore, it is important to check how the picture changes in physics Beyond the Standard Model (BSM) whenever the Higgs sector is extended or extra interactions for the SM Higgs boson are considered. New physics can impact the stability of the vacuum mainly in two ways. When new physics appears below the stability scale and it modifies the running of the couplings, this might even erase the possibility of a vacuum deeper than the EW one altogether. Even if the EW vacuum remains a false one, the tunneling time of the EW vacuum can be subject to higher dimensional operators in the UV [3].

Recently, the measured values of the muon $(g-2)_\mu$ [4, 5] and the W boson mass m_W [6] have both indicated significant deviations from the SM predictions [7], that we will refer to as the SM anomalies in the following, and have motivated the search for an explanation within extensions of the SM with extra particles and symmetries. However, it has been recently shown that the SM prediction for the muon $g-2$ based on the lattice results is consistent with its experimental value [8, 9]. Furthermore, the recent CMD-3 data [10] shows a sizable deviation from the other e^+e^- data, which were used to derive the SM prediction for the muon $g-2$ in the dispersive approach taken in Ref. [7]. Thus, it is important to understand the hadronic contributions to the muon $g-2$ well within the SM and there is a need of improvements on the experimental data. Nonetheless, it becomes of interest to investigate what the impact of new physics on the stability issue is in the phenomenologically motivated models as discussed above and provide more information from the complementary tests of new physics.

In this article, we revisit a lepton portal model with an extra $U(1)'$ gauge symmetry from this perspective, and perform an RG analysis to investigate on its stability. In this model, suggested by some of the authors [11], an $SU(2)_L$ singlet vector-like lepton charged under $U(1)'$ is introduced. The vector-like lepton mixes with the muon through the vacuum expectation values (VEVs) of an extra Higgs doublet and a dark Higgs field, leading to a small seesaw mass for the muon. The muon $g-2$ can be explained thanks to extra one-loop corrections coming from the vector-lepton and the Z' boson, while the W mass m_W can be increased, at the same time, through a tree-level mixing between the Z boson and the Z' boson when the Z' is heavier than Z . As the muon $g-2$ anomaly favors the $U(1)'$ breaking scale to be below about 200 GeV, the extra gauge coupling required to increase m_W tends to be large [11], so that it can have a strong impact on the RG flow of the theory. There are previous analyses of RG equations and Higgs vacuum stability in the extended models with

vector-like leptons and extended Higgs sectors with a motivation to explain the muon $g - 2$ anomaly [12, 13]. In our work, making a complete study of the one-loop RG equations in our model, we aim to go beyond the limited discussion on loop corrections done in the previous work in Ref. [11]. As a result, we present new results on the stability and the Landau pole of the model in the parameter space favored by both the muon $g - 2$ and W boson mass anomalies. However, in view of the recent lattice results for the muon $g - 2$, it is notable that our RG analysis is not limited to the parameter space for the muon $g - 2$ anomaly.

Setting the couplings of the Z' boson and of the vector-like lepton at low energy to explain the SM anomalies, we perform the RG analysis of the model. Following [11], we first consider the alignment limit of the Higgs potential by choosing some particular relations between the quartic couplings in the extended Higgs sector and identify the Landau pole and the scale where perturbativity is lost. We then extend the RG analysis to more general cases with “minimal relations” between the quartic couplings, i.e. imposing only the relations needed to reproduce the experimental constraints and allowing for a misalignment between the CP-even neutral components of the Higgs doublets. The results of our analysis allow to determine a region of parameter space where the SM anomalies can be explained, the Landau pole of the theory is sufficiently higher than the scales experimentally probed so far, making it possible for the theory to have a UV cutoff at high enough scales, and the running of the quartic coupling can be lifted to positive values to (possibly) stabilize the vacuum.

The paper is organized as follows. We present the model setup and the lepton portal interactions of the vector-like lepton in section 2. We then consider the phenomenological constraints from the SM anomalies as well as Z' searches at the Large Hadron Collider (LHC) in section 3. Next we provide the analysis of vacuum stability and perturbativity with the running couplings in the model, focusing on the alignment limit of the extended Higgs potential and the low-energy inputs from the SM anomalies in section 4. We discuss the RG analysis for more general cases where the Higgs quartic couplings are deviated from the alignment limit and more general conditions for decoupling the dark Higgs boson are considered in section 5. There are two appendices where we present the calculation of the effective mass matrices for scalars, gauge bosons and fermions in this model and of the RG equations. Finally, conclusions are drawn.

2 The model

Besides the SM fields, our model consists of an $SU(2)_L$ singlet vector-like lepton E , a second Higgs doublet H' and a dark Higgs field ϕ , all charged under a $U(1)'$ gauge group, whose gauge boson we denote with Z' [11, 14, 15]. The $U(1)'$ charge assignments are summarized in Table 1. The charges of the BSM fields are taken to be $+2$ or -2 for simplicity, but different choices for the charges can be made rescaling the $g_{Z'}$ coupling.

	q_L	u_R	d_R	l_L	e_R	H	H'	E_L	E_R	ϕ
$U(1)'$	0	0	0	0	0	0	+2	-2	-2	-2

Table 1: The $U(1)'$ charges for the SM and extra fields.

The Lagrangian for the electroweak sector, including the new fields we introduce, reads

$$\begin{aligned} \mathcal{L} = & -\frac{1}{4}W_{\mu\nu}^a W^{a\mu\nu} - \frac{1}{4}B_{\mu\nu}B^{\mu\nu} - \frac{1}{4}F'_{\mu\nu}F'^{\mu\nu} - \frac{\sin\xi}{2}F'_{\mu\nu}B^{\mu\nu} \\ & + |D_\mu\phi|^2 + |D_\mu H'|^2 + |D_\mu H|^2 - V(\phi, H, H') + \mathcal{L}_{\text{fermions}}, \end{aligned} \quad (1)$$

with

$$\begin{aligned} \mathcal{L}_{\text{fermions}} = & \sum_{i=\text{SM}, E} i\bar{\psi}_i\gamma^\mu D_\mu\psi_i - y_d\bar{q}_L d_R H - y_u\bar{q}_L u_R \tilde{H} - y_l\bar{l}_L e_R H \\ & - M_E\bar{E}E - \lambda_E\phi\bar{E}_L e_R - y_E\bar{l}_L E_R H' + \text{h.c.} . \end{aligned} \quad (2)$$

Here, $\tilde{H} = i\sigma^2 H^*$, $F'_{\mu\nu}$ is the $U(1)'$ field strength, and the covariant derivatives for BSM fields are

$$\begin{aligned} D_\mu\phi &= (\partial_\mu + 2ig_{Z'}Z'_\mu)\phi, \\ D_\mu H' &= \left(\partial_\mu - 2ig_{Z'}Z'_\mu - \frac{1}{2}ig_Y B_\mu - \frac{1}{2}ig\sigma^i W_\mu^i\right)H', \\ D_\mu E &= (\partial_\mu + 2ig_{Z'}Z'_\mu + ig_Y B_\mu)E. \end{aligned} \quad (3)$$

In particular, the dark Higgs ϕ is charged only under $U(1)'$, while the vector-like lepton is charged under both $U(1)'$ and $U(1)_Y$, and the second Higgs doublet has the same quantum numbers as the SM Higgs except for its $U(1)'$ charge. The potential $V(\phi, H, H')$ is taken as¹

$$\begin{aligned} V(\phi, H, H') = & \mu_1^2 H^\dagger H + \mu_2^2 H'^\dagger H' - (\mu_3\phi H^\dagger H' + \text{h.c.}) \\ & + \lambda_1(H^\dagger H)^2 + \lambda_2(H'^\dagger H')^2 + \lambda_3(H^\dagger H)(H'^\dagger H') + \lambda_4(H^\dagger H')(H'^\dagger H) \\ & + \mu_\phi^2\phi^*\phi + \lambda_\phi(\phi^*\phi)^2 + \lambda_{H\phi}H^\dagger H\phi^*\phi + \lambda_{H'\phi}H'^\dagger H'\phi^*\phi. \end{aligned} \quad (4)$$

In the “normal” vacuum where the electroweak symmetry and the $U(1)'$ symmetry are broken, we take

$$H = \frac{1}{\sqrt{2}} \begin{pmatrix} 0 \\ v_1 \end{pmatrix}, \quad H' = \frac{1}{\sqrt{2}} \begin{pmatrix} 0 \\ v_2 \end{pmatrix}, \quad \phi = \frac{v_\phi}{\sqrt{2}}. \quad (5)$$

¹Other quartic couplings, λ_5 , λ_6 and λ_7 , in two Higgs doublet models [16], are forbidden by the $U(1)'$ symmetry under which the second Higgs doublet H' transforms.

A mass mixing between the Z and Z' gauge bosons arises in such a vacuum [11, 14, 15, 17]. The mass matrix for the charged lepton (muon) and the vector-like lepton [11] is defined from

$$\begin{aligned}\mathcal{L}_{L,\text{mass}} &= -M_E \bar{E}E - m_0 \bar{e}e - (m_R \bar{E}_L e_R + m_L \bar{e}_L E_R + \text{h.c.}) \\ &= -(\bar{e}_L, \bar{E}_L) \mathcal{M}_L \begin{pmatrix} e_R \\ E_R \end{pmatrix} + \text{h.c.},\end{aligned}\quad (6)$$

with

$$\mathcal{M}_L = \begin{pmatrix} m_0 & m_L \\ m_R & M_E \end{pmatrix}.\quad (7)$$

Here, m_0 is the bare lepton mass given by $m_0 = \frac{1}{\sqrt{2}} y_l v_1$, and m_R, m_L are the mixing masses, given by $m_R = \frac{1}{\sqrt{2}} \lambda_E v_\phi$ and $m_L = \frac{1}{\sqrt{2}} y_E v_2$, respectively. In the limit of $m_0, m_R, m_L \ll M_E$, the mass eigenvalues for the leptons can be expressed as

$$m_{l_2} \simeq M_E, \quad m_{l_1} \approx m_0 - \frac{m_R m_L}{M_E},\quad (8)$$

while the mixing angles for the right-handed and left-handed leptons [11] become

$$\theta_R \simeq \frac{m_R}{M_E}, \quad \theta_L \simeq \frac{m_L}{M_E}.\quad (9)$$

Therefore, for $m_0 \gtrsim \frac{m_R m_L}{M_E}$ we get a seesaw mass contribution for the charged lepton [11] as $\frac{m_R m_L}{M_E} \simeq \theta_R \theta_L M_E$. A similar lepton-portal model with $SU(2)_D$ was considered for muon seesaw mass, muon $g-2$ as well as W boson mass [18].

3 Phenomenological constraints on Z'

As will be shown in Sec. 4.5, in order to explain the muon $g-2$ experimental anomaly with our model while avoiding the appearance of a Landau pole at too low energies, a small $g_{Z'}$ (correspondingly, a weak-scale Z' boson mass) are necessary. For such a scenario, the LHC searches for additional Z' gauge bosons should be taken into account.

3.1 SM anomalies: muon $g-2$ and W boson mass

The dominant corrections to the muon $g-2$ in our model arise from the one-loop vector-like lepton and Z' gauge boson contributions. In the limit $M_E \gg m_{Z'}$, the correction reads [11]

$$\Delta a_\mu \simeq \frac{1}{4\pi^2} \frac{g_{Z'}^2 m_\mu^2}{m_{Z'}^2},\quad (10)$$

with $m_{Z'}^2 = 4g_{Z'}^2 (v_\phi^2 + v^2 \sin^2 \beta)$, so that Δa_μ becomes independent of the value of $g_{Z'}$. When $v_\phi^2 \gg v^2 \sin^2 \beta$, $m_{Z'}^2 \simeq 4g_{Z'}^2 v_\phi^2$ and we only need to fix the VEV of the singlet scalar v_ϕ to

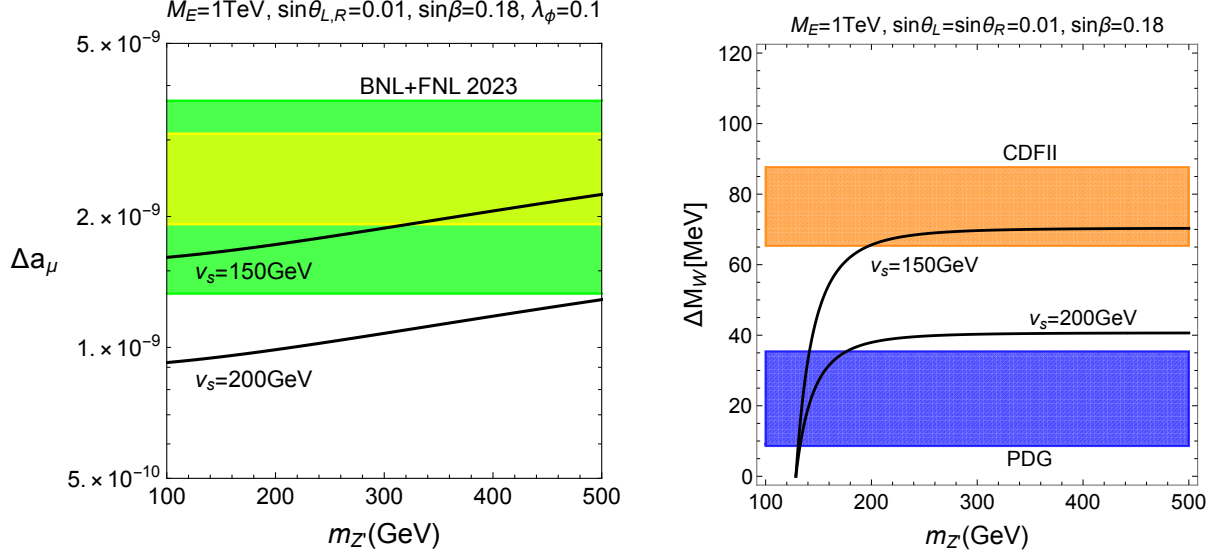


Figure 1: The corrections to the muon $g - 2$ (left plot) and the W boson mass (right plot) as a function of $m_{Z'}$. We fixed $M_E = 1 \text{ TeV}$, $\sin\theta_L = \sin\theta_R = 0.01$, $\sin\beta = 0.18$ and $\lambda_\phi = 0.1$. The 1σ and 2σ contours of the deviation of the muon $g - 2$ from the combined experimental value of BNL and FNL 2023 is shown in yellow and green regions, respectively, and the 1σ values of the deviation of the W boson mass are shown in orange and blue regions for CDFII and PDG world average, respectively.

fit the muon $g - 2$. On the other hand, the correction to the W boson mass in our model stems from the tree-level mixing between the Z and Z' gauge bosons, and for $m_{Z'} \gg m_Z$ it is approximated by

$$\Delta m_W \simeq \frac{8}{(c_W^2 - s_W^2)} \frac{g_{Z'}^2 m_Z^2}{g_Y^2 m_{Z'}^2} \sin^4 \beta. \quad (11)$$

From $g_{Z'}^2/m_{Z'}^2 \simeq 1/(4v_\phi^2)$ it is immediately understood that, in this limit, the correction to the W boson mass becomes independent of $g_{Z'}$, too. As $m_{Z'}$ gets closer to m_Z , however, the above approximation breaks down, so the smaller $g_{Z'}$ (or $m_{Z'}$), the smaller the correction to m_W .

We comment on how flexible the parameter space is to explain the muon $g - 2$ and W boson mass anomalies. In the left plot of Fig. 1, we depict the one-loop correction to the muon $g - 2$ as a function of $m_{Z'}$ in our model, with $v_s = v_\phi/\sqrt{2} = 200 \text{ GeV}$ and 150 GeV . We set the parameters of the vector-like lepton sector to $M_E = 1 \text{ TeV}$, $\sin\theta_L = \sin\theta_R = 0.01$, and choose $\sin\beta = 0.18$ and $\lambda_\phi = 0.1$ [11]. In the right plot of Fig. 1, we also show the tree-level correction to the W boson mass due to the Z - Z' mixing as a function of $m_{Z'}$, with $v_s = v_\phi/\sqrt{2} = 200 \text{ GeV}$ and 150 GeV , making the same choice for the other parameters as in the previous case. We note that in the case of $v_s = 200 \text{ GeV}$, new contributions to the muon $g - 2$ in our model are in tension with the experimental value at 2σ for the SM prediction based on Ref. [7], but they can be consistent with the recent lattice results [9] at 2σ . Thus, the parameter choices for Fig. 1 are compatible with the SM predictions appearing in the literature, so they will be taken for the later analysis on RG equations.

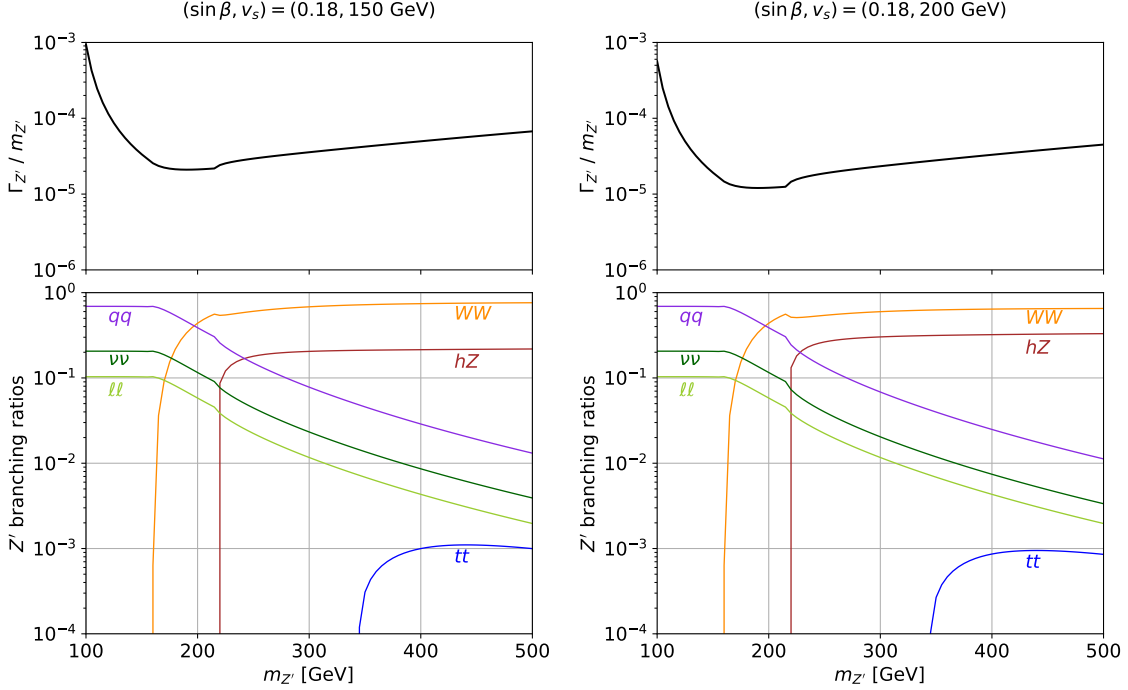


Figure 2: Ratio of Z' total width to its mass and Z' branching ratios as a function of Z' mass, for the dark Higgs VEV of $v_s = 150$ GeV (left) and $v_s = 200$ GeV (right), respectively. We take $\sin \beta = 0.18$; qq , ll , and $\nu\nu$ include five flavors of quarks, three flavors of leptons, and three flavors of neutrinos, respectively.

As a result, we find that a smaller value of v_s , for instance, $v_s = 150$ GeV, is favoured to explain the muon $g - 2$ within 1σ or 2σ levels, as shown in the left plot of Fig. 1. For the same value of v_s , we can explain the W boson mass reported by CDFII for a wide range of Z' boson masses, as shown in the right plot of Fig. 1. For a larger value of v_s , for instance $v_s = 200$ GeV, we can still explain the W boson mass anomaly from CDFII by taking a mild increase in $\sin \beta$ from 0.18, as far as $m_{Z'} \gtrsim 200$ GeV [11].

3.2 Z' signatures at the LHC

For a relatively light Z' boson, i.e. $m_{Z'} \sim 200 - 500$ GeV, dilepton final states become crucial for LHC phenomenology. We show the Z' production cross section from pp collisions at 13 TeV and the branching fractions of the Z' boson for the current LHC constraints and prospects. We assume the extra Higgs boson and the dark Higgs boson to have large enough masses so that their production from a Z' decay is kinematically forbidden. We employ MadGraph5_aMC@NLO [19] to calculate the cross sections and branching ratios of the Z' , while the model is implemented with FeynRules [20].

We begin by discussing the Z' boson decays. The $Z - Z'$ mass mixing allows the Z' to decay into states coupled to the Z with a suppression factor determined by the $Z - Z'$ mixing angle $\sin \zeta$; the decay width is then suppressed by a factor $\sin^2 \zeta$. When kinemat-

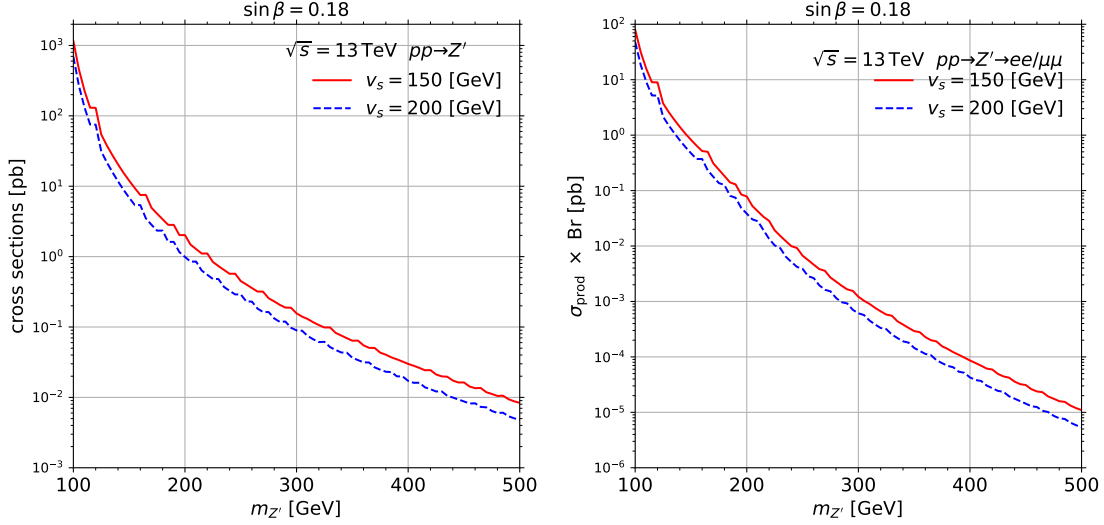


Figure 3: Total cross sections for Z' productions (left) and for Z' productions multiplied by a branching ratio to dilepton (ee and $\mu\mu$) (right) at the 13 TeV LHC as a function of Z' boson mass. Two choices of v_s are considered: 150 GeV shown as a red solid line and 200 GeV shown as a blue dashed line.

ically allowed, then, the WW , hZ , and tt channels open. The $U(1)'$ charge of the second Higgs determines an additional interaction for hZ final states, i.e. a $Z'-Z-h$ vertex whose corresponding width is not suppressed by the Z mass mixing angle, but by a $\sin^4 \beta$ factor. The $Z'-Z-h$ interaction Lagrangian is

$$\mathcal{L}_{Z'-Z-h} = Z'^\mu Z_\mu h v \frac{\sec \theta_w}{4} \left(\sec \theta_w \sin 2\zeta \left(g^2 + 4g_{Z'}^2 (\cos 2\beta - 2 \sin^2 \beta \cos 2\theta_w) - 4g_{Z'}^2 \right) - 8g g_{Z'} \sin^2 \beta \cos 2\zeta \right). \quad (12)$$

Here, θ_w is the Weinberg angle. Figure 2 shows the Z' total width scaled by the mass, $\Gamma_{Z'}/m_{Z'}$, and the decay branching ratios for the case where only decays to SM particles are allowed. We take $\sin \beta = 0.18$ and $v_s = 150$ GeV (in the left plot) or $v_s = 200$ GeV (in the right plot) as benchmark points. The qq , ll , and $\nu\nu$ channels include five flavors of quarks, three flavors of leptons, and three flavors of neutrinos, respectively. We see that, in addition to the dilepton channel, the WW and hZ channels are important (actually, the dominant ones) when kinematically allowed. The resonance is always very narrow ($\Gamma_{Z'}/m_{Z'} < 0.1\%$), and, as long as $m_{Z'} \lesssim 2m_w$, $\Gamma_{Z'}/m_{Z'}$ drops as $m_{Z'}$ increases due to the decrease of the $Z-Z'$ mixing.

Let us now discuss the Z' production and its decay to the dilepton state. The Z' production cross sections (left) and Z' production cross sections multiplied by the ee and $\mu\mu$ dilepton branching ratio (right) for pp collision at 13 TeV are depicted in Fig. 3 as a function of $m_{Z'}$. The opening of the WW and hZ channels is such that the dilepton production is suppressed strongly for large enough values of $m_{Z'}$, for e.g. it is less than 1 fb for $m_{Z'} \gtrsim 300$ GeV.

With the results of ATLAS for dilepton final states at the 13 TeV LHC run with integrated luminosity $L_{\text{int}} = 139/\text{fb}$ [21], parametric regions with $m_{Z'} \gtrsim 300$ GeV and $\sin \beta = 0.18$

are allowed in our scenario. As we have seen, within this parametric region the WW and hZ final states are dominant, and these resonant boson productions are safe with respect to the $L_{\text{int}} = 139/\text{fb}$, 13 TeV LHC results [22–25]. As the LHC constraints on dileptons are quite severe, dilepton final state produced from Z' boson resonance around $m_{Z'} \sim 300$ GeV should be targeted by the next LHC results. The same considerations hold for WW final states for $m_{Z'} \gtrsim 300$ GeV, with the latter being dominant within our scenario.

4 SM anomalies and running couplings

We begin by discussing some conditions that the scalar potential must satisfy at tree level, and we later consider the one-loop effective potential. Fixing the low-energy parameters to explain the SM anomalies and taking the alignment limit for the Higgs quartic couplings, we undertake the RG analysis of the model, and in particular of the quartic couplings, and identify the Landau pole and the perturbativity scale.

4.1 Tree-level stability of the potential

The potential $V(\phi, H, H')$ in eq. (4) has a rich vacuum structure, with CP-breaking and charge-breaking minima, besides CP-even and neutral ones (that we will refer to as “normal” ones from now on). To derive the conditions under which a normal vacuum can develop, we parametrize the fields in the following way [26]:

$$|H| = \chi_1, \quad |H'| = \chi_2, \quad H^\dagger H' = \chi_1 \chi_2 \rho e^{i\theta}, \quad \phi = \phi_1 e^{i\varphi}. \quad (13)$$

From the inequality $|H^\dagger H'| \leq |H||H'|$, ρ is $\rho \in [-1, 1]$. In terms of this new set of parameters, the potential (4) takes the form

$$V(\chi_1, \chi_2, \phi_1, \rho, \theta, \varphi) = \mu_1^2 \chi_1^2 + \mu_2^2 \chi_2^2 - 2\mu_3 \cos(\varphi + \theta) \phi_1 \rho \chi_1 \chi_2 + \lambda_1 \chi_1^4 + \lambda_2 \chi_2^4 + \lambda_3 \chi_1^2 \chi_2^2 + \lambda_4 \chi_1^2 \chi_2^2 \rho^2 + \mu_\phi^2 \phi_1^2 + \lambda_\phi \phi_1^4 + \lambda_{H\phi} \chi_1^2 \phi_1^2 + \lambda_{H'\phi} \chi_2^2 \phi_1^2, \quad (14)$$

and its extremization conditions are then

$$\begin{cases} (\mu_1^2 + 2\lambda_1 \chi_1^2 + \lambda_3 \chi_2^2 + \lambda_4 \rho^2 \chi_2^2 + \lambda_{H\phi} \phi_1^2) \chi_1 - \mu_3 \cos(\varphi + \theta) \rho \phi_1 \chi_2 = 0, \\ (\mu_2^2 + 2\lambda_2 \chi_2^2 + \lambda_3 \chi_1^2 + \lambda_4 \rho^2 \chi_1^2 + \lambda_{H'\phi} \phi_1^2) \chi_2 - \mu_3 \cos(\varphi + \theta) \rho \phi_1 \chi_1 = 0, \\ (\mu_\phi^2 + 2\lambda_\phi \phi_1^2 + \lambda_{H\phi} \chi_1^2 + \lambda_{H'\phi} \chi_2^2) \phi_1 - \mu_3 \cos(\varphi + \theta) \rho \chi_1 \chi_2 = 0, \\ \lambda_4 \chi_1^2 \chi_2^2 \rho - \mu_3 \cos(\varphi + \theta) \phi_1 \chi_1 \chi_2 = 0, \\ \sin(\varphi + \theta) \phi_1 \rho \chi_1 \chi_2 = 0. \end{cases} \quad (15)$$

When $\phi_1, \rho, \chi_1, \chi_2 \neq 0$, the last equation is solved by $\sin(\varphi + \theta) = 0$, from which $\cos(\varphi + \theta) = \pm 1$. When $\mu_3 \phi_1 \rho \chi_1 \chi_2 > 0$, the upper sign minimizes the potential and the lower sign maximizes it. The opposite is true for $\mu_3 \phi_1 \rho \chi_1 \chi_2 < 0$.

Let us now concentrate on the value of ρ that minimizes the potential. We start with the case $\mu_3 \phi_1 \rho \chi_1 \chi_2 > 0$, and thus $\cos(\varphi + \theta) = 1$. For a positive λ_4 , the $\lambda_4 \chi_1^2 \chi_2^2 \rho^2$ contribution in

the potential is necessarily positive and contrasts the negative contribution given by μ_3 . The value of ρ at the minimum is given by the solution to eq. (15)₄ (keeping in mind that $|\rho| \leq 1$). On the contrary, when $\lambda_4 < 0$, the $\lambda_4 h_1^2 h_2^2 \rho^2$ contribution is necessarily negative. It adds up with the negative contribution coming from the μ_3 term. In this case, the minimum is found for $\rho = \pm 1$, and the solution to (15)₄ maximizes the potential. When $\mu_3 \phi_1 \rho \chi_1 \chi_2 < 0$, we should take $\cos(\varphi + \theta) = -1$. As a consequence, the contribution from μ_3 is again negative, and the same observations as those made in the $\mu_3 \phi_1 \rho \chi_1 \chi_2 > 0$ case apply.

The normal vacuum in eq. (5) corresponds to $h_1^2 = v_1^2/2$, $h_2^2 = v_2^2/2$, $\rho = 1$, $\theta = 2\pi n$, $\phi_1^2 = v_\phi^2/2$, $\varphi = 2\pi n$. In particular, we have $h_1, h_2, \phi_1, \rho > 0$ and $\cos(\varphi + \theta) = 1$. Then, from the above discussion, it is immediate to deduce that there are two scenarios where the configuration for the normal vacuum in eq. (5) can appear as a minimum of the potential: when $\mu_3 > 0$ and $\lambda_4 < 0$, or when $\mu_3 > 0$, $\lambda_4 > 0$ and the solution to (15)₄ gives $\rho = 1$. For this to happen, λ_4 must be $\lambda_4 = \sqrt{2}\mu_3 v_\phi / v_1 v_2$. As we will see in the following, the values of μ_3 , v_1 , v_2 and v_ϕ that we will be concerned with in our analysis are such that the vacuum solution with positive λ_4 is not of interest, as it would require too large values of λ_4 .

Our analysis will only be concerned with normal vacua, and, as usually done, we will parametrize the VEV of the two Higgs doublets as $v_1 = v \cos \beta$, $v_2 = v \sin \beta$, where v is the value of the Higgs VEV in the Standard Model. Concerning the other types of vacua mentioned above, let us remind that, as shown in [27–30], minima of a different nature cannot simultaneously coexist at tree-level in the 2HDM. Besides the impossibility of having minima of different nature at tree-level, it is well known that multiple non-degenerate vacua of the same nature can simultaneously coexist at tree-level in the 2HDM [31]. The parameter space must then be restricted to those regions where either the potential does not develop any minimum deeper than the electroweak-like one or, if it does develop such a minimum, the tunneling time from the electroweak-like vacuum is larger than the age of the Universe, $\tau \geq \tau_U$ [32]. The benchmark points that will be considered in our analysis do not develop any minimum different than the SM one at tree-level, and we do not need to worry about these issues. Stability of the potential will be investigated at the radiative (one-loop) level in the later discussion.

Tree-level stability of the potential requires that the quartic coupling matrix² (in the basis $(\chi_1^2, \chi_2^2, \phi_1^2)$),

$$\mathcal{M}_\lambda = \begin{pmatrix} \lambda_1 & \frac{\lambda_3 + \rho^2 \lambda_4}{2} & \frac{\lambda_{H\phi}}{2} \\ \frac{\lambda_3 + \rho^2 \lambda_4}{2} & \lambda_2 & \frac{\lambda_{H'\phi}}{2} \\ \frac{\lambda_{H\phi}}{2} & \frac{\lambda_{H'\phi}}{2} & \lambda_\phi \end{pmatrix}, \quad (16)$$

is copositive definite [26]. This gives the conditions

$$\begin{cases} \lambda_1 \geq 0, & \lambda_2 \geq 0, & \lambda_\phi \geq 0, \\ \lambda_3 + \rho^2 \lambda_4 + 2\sqrt{\lambda_1 \lambda_2} \geq 0, & \lambda_{H\phi} + 2\sqrt{\lambda_1 \lambda_\phi} \geq 0, & \lambda_{H'\phi} + 2\sqrt{\lambda_2 \lambda_\phi} \geq 0, \end{cases} \quad (17)$$

²In the following equations, we keep a generic ρ . For the normal background configurations considered in this work, ρ is $\rho = 1$.

and

$$\begin{aligned} & \sqrt{\lambda_1 \lambda_2 \lambda_\phi} + \frac{\lambda_3 + \rho^2 \lambda_4}{2} \sqrt{\lambda_\phi} + \frac{\lambda_{H\phi}}{2} \sqrt{\lambda_2} + \frac{\lambda_{H'\phi}}{2} \sqrt{\lambda_1} \\ & + \frac{1}{2} \sqrt{(\lambda_3 + 2\sqrt{\lambda_1 \lambda_2})(\lambda_{H\phi} + 2\sqrt{\lambda_1 \lambda_\phi})(\lambda_{H'\phi} + 2\sqrt{\lambda_2 \lambda_\phi})} \geq 0. \end{aligned} \quad (18)$$

Having in mind the typical RG improvement of the potential, in the remainder we will study radiative stability of the potential at the one-loop level by requiring that the above conditions (17), (18) are satisfied with the running couplings $\lambda_i(\mu)$.

4.2 One-loop effective potential

The gauge structure of the model is such that the scalar degrees of freedom can be restricted from 10 to 6. As we are only interested in a specific type of configurations and want to study the potential only in the subspace of neutral CP-even scalars, we further restrict the problem to a 3-field problem.

We parametrize the doublets and the scalar singlet as

$$H = \begin{pmatrix} \phi_1^+ \\ \frac{1}{\sqrt{2}}(h_1 + \rho_1 + i\eta_1) \end{pmatrix}, \quad (19)$$

$$H' = \begin{pmatrix} \phi_2^+ \\ \frac{1}{\sqrt{2}}(h_2 + \rho_2 + i\eta_2) \end{pmatrix}, \quad (20)$$

$$\phi = \frac{1}{\sqrt{2}}(s + \rho_3 + i\eta_3) \quad (21)$$

where h_1, h_2, s are the background fields of which we want to study the potential³. The mass matrices obtained in the (h_1, h_2, s) background (actually, in a slightly more general background) are easily calculated and are reported in Appendix A.

The tree-level potential for h_1, h_2 and s is obtained straightforwardly from the expansion of (4),

$$\begin{aligned} V_0(h_1, h_2, s) = & \frac{\mu_1^2}{2} h_1^2 + \frac{\mu_2^2}{2} h_2^2 + \frac{\mu_\phi^2}{2} s^2 + \frac{\lambda_1}{4} h_1^4 + \frac{\lambda_2}{4} h_2^4 + \frac{\lambda_\phi}{4} s^4 \\ & + \frac{\lambda_3 + \lambda_4}{4} h_1^2 h_2^2 + \frac{\lambda_{H\phi}}{4} h_1^2 s^2 + \frac{\lambda_{H'\phi}}{4} h_2^2 s^2 - \frac{\mu_3}{\sqrt{2}} h_1 h_2 s. \end{aligned} \quad (22)$$

Performing the typical loop integral with the mass terms $\mathcal{M}_i(h_1, h_2, s)$ and indicating with Λ the cutoff of the theory, we obtain in the physically meaningful limit $\Lambda^2 \gg M_i^2$ (M_i indicate

³As discussed in the Appendix, to distinguish contributions that renormalize the $|H|^2|H'|^2$ operator from contributions that renormalize the $|H^\dagger H'|^2$ operator, we need to consider a slightly more complicated background configuration, where at least one of the doublets develop an upper component. The (h_1, h_2, s) background of equations (19)-(21) can be re-obtained taking the limit for the upper component to vanish after renormalization is performed and renormalization group equations have been determined.

the eigenvalues of the mass matrices)

$$V_{1l} = \sum_i (-1)^{\delta_{f,i}} n_i \frac{\text{Tr}(\mathcal{M}_i^2)}{32\pi^2} \Lambda^2 + \sum_i (-1)^{\delta_{f,i}} \frac{n_i}{64\pi^2} \text{Tr} \mathcal{M}_i^4 \left(\log \left(\frac{\mathcal{M}_i^2}{\Lambda^2} \right) - \frac{1}{2} \right) + \mathcal{O}(\Lambda^{-1}), \quad (23)$$

where $n_i = 12$ for the top quark, $n_i = 4$ for the VLL-muon fermion mass matrix (A.28), $n_i = 3$ for the gauge mass matrix (A.25) and $n_i = 1$ for the scalar one (A.5). If we write the quadratic contribution in Λ as $\frac{1}{2}(\alpha_1 h_1^2 + \alpha_2 h_2^2 + \alpha_\phi s^2) \Lambda^2$, we have

$$\begin{cases} \alpha_1 = \frac{9g^2}{64\pi^2} + \frac{3g_Y^2}{64\pi^2} + \frac{3\lambda_1}{8\pi^2} + \frac{\lambda_3}{8\pi^2} + \frac{\lambda_4}{16\pi^2} + \frac{\lambda_{H\phi}}{16\pi^2} - \frac{y_l^2}{8\pi^2} - \frac{3y_t^2}{8\pi^2}, \\ \alpha_2 = \frac{9g^2}{64\pi^2} + \frac{3g_Y^2}{64\pi^2} + \frac{3g_{Z'}^2}{4\pi^2} + \frac{3\lambda_2}{8\pi^2} + \frac{\lambda_3}{8\pi^2} + \frac{\lambda_4}{16\pi^2} + \frac{\lambda_{H'\phi}}{16\pi^2} - \frac{y_E^2}{8\pi^2}, \\ \alpha_3 = \frac{3g_{Z'}^2}{4\pi^2} + \frac{\lambda_\phi}{4\pi^2} + \frac{\lambda_{H\phi}}{8\pi^2} + \frac{\lambda_{H'\phi}}{8\pi^2} - \frac{\lambda_E^2}{8\pi^2}. \end{cases} \quad (24)$$

In the above equations we kept the contributions from the muon Yukawa coupling y_l . The reason we keep terms proportional to y_l in our calculation is that the latter enters in the mass matrix that describes the mixing between the muon and the vector-like lepton. As such, it might happen that y_l appears in combination with other couplings that enhance its contribution.

The Renormalization Group Equations (RGEs) are conveniently extracted requiring independence from Λ of the full effective potential at the one-loop level, $V = V_0 + V_{1l}$, namely,

$$\Lambda \frac{d}{d\Lambda} V = 0 \rightarrow \left(\Lambda \frac{\partial}{\partial \Lambda} + \mu_i^2 \gamma_{\mu_i^2} \frac{\partial}{\partial \mu_i^2} + \beta_{\mu_3} \frac{\partial}{\partial \mu_3} + \beta_{\lambda_i} \frac{\partial}{\partial \lambda_i} - \gamma_i \phi_i \frac{\partial}{\partial \phi_i} \right) V = 0 \quad (25)$$

where i runs over h_1, h_2, s while β and γ indicate the beta functions and anomalous dimensions, respectively. We show the various RGEs extracted from this equation, together with all the other necessary RGEs, in Appendix B.

To implement the fact that the contribution from a state of running mass $m(\mu)$ is approximately frozen at scales μ below $m(\mu)$ [33], we supplement the RGEs found from the one-loop calculations, and presented in Appendix B, with threshold corrections in the form of the Heaviside theta function $\theta(\mu^2 - m^2(\mu))$.

4.3 Conditions from SM anomalies

Taking into account the parameter space motivated by both the muon $g - 2$ and the W boson mass in Ref. [11], we consider the following set of boundary values at low energy⁴:

$$\left\{ \begin{array}{l} M_E = 1 \text{ TeV}, \\ \sin \beta = 0.18, \\ \sin \theta_L = 0.01 \rightarrow y_E = 0.32, \\ \sin \theta_R = 0.011 \rightarrow \begin{cases} \text{if } v_\phi = \sqrt{2} \times 200 \text{ GeV} \rightarrow \lambda_E = 0.055; \\ \text{if } v_\phi = \sqrt{2} \times 150 \text{ GeV} \rightarrow \lambda_E = 0.073, \end{cases} \\ m_{Z'} = 500 \text{ GeV} \rightarrow \begin{cases} \text{if } v_\phi = \sqrt{2} \times 200 \text{ GeV} \rightarrow g_{Z'} = 0.87; \\ \text{if } v_\phi = \sqrt{2} \times 150 \text{ GeV} \rightarrow g_{Z'} = 1.15. \end{cases} \end{array} \right.$$

Here, we took two cases for the VEV of the singlet scalar, $v_s = v_\phi/\sqrt{2} = 200 \text{ GeV}$ and $v_s = 150 \text{ GeV}$. From $m_{Z'}^2 = 4g_{Z'}^2 (v^2 \sin^2 \beta + v_\phi^2)$, which is the diagonal term of the neutral gauge boson mass matrix \mathcal{M}_Z^2 in the Z' direction, we can determine $g_{Z'}$ for given $\sin \beta$ and $m_{Z'}$. Moreover, we can also determine λ_E for seesaw muon mass.

We now list up the procedure for determining the boundary values of the rest of the parameters in our model. From $m_W = gv/2$, the IR boundary condition for g is the same as in the SM. Concerning the Z boson, $m_Z = \sqrt{g^2 + g_Y^2} v/2$ is the diagonal term of the \mathcal{M}_Z^2 matrix in the Z direction. The boundary value for g_Y is found imposing that the smaller eigenvalue of \mathcal{M}_Z^2 is the measured Z mass. Finally, since the top and the muon only couple to h_1 , but not to h_2 , the bare mass terms generated by the scalar VEVs for them are $m_t = y_t v_1/\sqrt{2}$ and $m_l = y_l v_1/\sqrt{2}$, respectively. This means that the boundary conditions for y_t and y_l are not the same as in the SM, but are rather magnified by a factor $\cos^{-1} \beta$. We note that the seesaw mass generated by the mixing with the vector-like lepton gives a negative contribution to the muon mass⁵ [11], so y_l can be larger than the one in the SM. To avoid a significant tuning for the muon mass, we keep y_l of order similar to the SM one, namely $y_l = y_l^{(\text{SM})} \cos^{-1} \beta$.

After imposing the above phenomenological constraints, we still have the remaining 11 parameters to fix: $\mu_1, \mu_2, \mu_\phi, \lambda_1, \lambda_2, \lambda_\phi, \lambda_3, \lambda_4, \lambda_{H\phi}, \lambda_{H'\phi}, \mu_3$. To proceed further, we continue to follow [11] and take the following steps.

Some of the non-diagonal terms of the scalar mass matrix \mathcal{M}_H^2 (see Eq. (A.5) and the following discussion), namely, $M_{H,13}^2$ and $M_{H,23}^2$, can be put to zero in the vacuum (v_1, v_2, v_ϕ) by the convenient choice,

$$\lambda_{H\phi} = \frac{\mu_3 \tan \beta}{\sqrt{2}v_\phi}, \quad \lambda_{H'\phi} = \frac{\mu_3 \cot \beta}{\sqrt{2}v_\phi}. \quad (26)$$

⁴As compared to Ref. [11], we use the convention $\phi = (s + i\eta_3)/\sqrt{2}$. Accordingly, the vacuum value of ϕ, v_ϕ , in our work, corresponds to $\sqrt{2}$ times the vacuum value of ϕ in [11].

⁵In the seesaw limit, the lowest eigenvalue of the fermion mass matrix is $m_{l_1} \sim m_0 - \frac{m_R m_L}{M_E}$. The symbols m_0, m_R and m_L are defined in Appendix A.

These conditions decouple the dark Higgs ϕ from the two Higgs doublets H and H' . With this choice, the third minimization condition in (15) reads $\mu_\phi^2 + \lambda_\phi v_\phi^2 = 0$, and $M_{H,33}^2$ gives rise to the mass eigenvalue for the singlet scalar,

$$m_\phi^2 \equiv M_{H,33}^2 = 2\lambda_\phi v_\phi^2 + \frac{\mu_3}{2\sqrt{2}} \sin(2\beta) \frac{v^2}{v_\phi}. \quad (27)$$

The 2×2 upper matrix of \mathcal{M}_H^2 , that we denote by $\widetilde{\mathcal{M}}_H^2$, can be simplified using the minimization equations in (15). It takes the form

$$\widetilde{\mathcal{M}}_H^2 = \begin{pmatrix} 2\lambda_1 v_1^2 + \frac{\mu_3}{\sqrt{2}} \tan \beta v_\phi & \lambda_{34} v_1 v_2 - \frac{\mu_3}{\sqrt{2}} v_\phi \\ \lambda_{34} v_1 v_2 - \frac{\mu_3}{\sqrt{2}} v_\phi & 2\lambda_2 v_2^2 + \frac{\mu_3}{\sqrt{2}} \cot \beta v_\phi \end{pmatrix}, \quad (28)$$

where we defined $\lambda_{34} \equiv \lambda_3 + \lambda_4$. Taking the $\tan \beta$ -independent solution for the alignment limit of the two doublets as in [11], that amounts to set the relations

$$\lambda_1 = \lambda_2 = \frac{\lambda_{34}}{2}, \quad (29)$$

among the quartic couplings, a further simplification arises. With this input, in fact, we get the eigenvalues of $\widetilde{\mathcal{M}}_H^2$ as⁶

$$m_{h_1}^2 = 2\lambda_1 v^2, \quad m_{h_2}^2 = \sqrt{2} \mu_3 v_\phi \sin^{-1}(2\beta). \quad (30)$$

To recover the SM Higgs in the decoupling limit of H' and ϕ , we identify the first of these two physical masses with the SM Higgs mass. Therefore, the boundary value of λ_1 (and consequently that of λ_2 and $\lambda_{34}/2$) is the same one as the boundary value for the Higgs quartic coupling in the SM. As first shown in [35] and further stressed in [11], it is interesting to observe that, when the above condition (29) is satisfied, the alignment of the two Higgs doublets is motivated by the fact that the H - H' scale invariant sector of the scalar potential is maximally symmetric.

The combination of all the relations and conditions described above leaves us with only three free independent parameters. We can conveniently choose them to be λ_ϕ , μ_3 and λ_3 . In fact, from $\mu_\phi^2 + \lambda_\phi v_\phi^2 = 0$ we see that the choice of λ_ϕ determines the value of μ_ϕ . The choice of μ_3 determines both $\lambda_{H\phi}$ and $\lambda_{H'\phi}$ from (26), and μ_1 and μ_2 from the minimization equations (15)₁ and (15)₂. Finally, the values of λ_3 and λ_4 are subject to the condition $\lambda_{34} = 2\lambda_1$, so that the choice of one fixes the other. As the dependence of the results on the choice of the couple (λ_3, λ_4) that realizes the condition $\lambda_{34} = 2\lambda_1$ is absolutely straightforward, in our investigation we will study the (λ_ϕ, μ_3) parameter space and, for each of the points in it, we will consider the choice $(\lambda_3, \lambda_4) = (2\lambda_1, 0)$. In this respect, we recall that, for consistency, λ_4 should be $\lambda_4 \leq 0$, so any other choice would have to be of the form $(\lambda_3, \lambda_4) = (2\lambda_1 + \delta, -\delta)$, with $\delta > 0$. It is easily seen that any admissible choice, that is any choice that keeps the couplings in the perturbative regime at sufficiently low energies, gives, for all practical reasons, the same results.

⁶For simplicity, below we use the same symbols as for the interaction eigenstate and indicate the mass eigenstates with h_1 and h_2 .

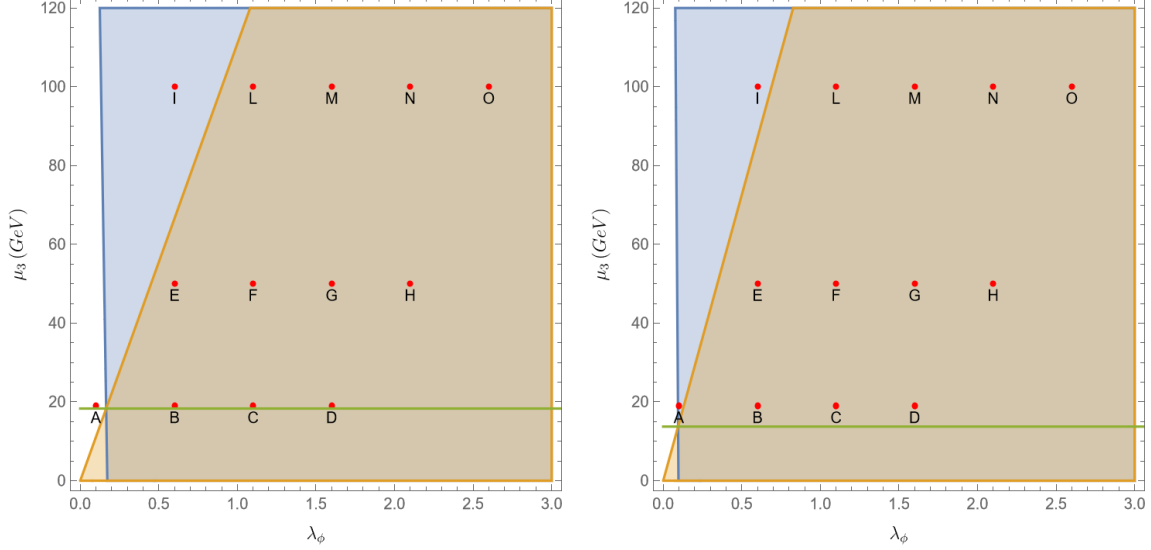


Figure 4: Benchmark points in the parameter space for λ_ϕ vs μ_3 . We chose $v_\phi = \sqrt{2} \times 150$ GeV on *left panel* and $v_\phi = \sqrt{2} \times 200$ GeV on *right panel*. In both panels, the blue region indicates the portion of parameter space where the second condition in (31) ($m_s \geq m_{h_1}$) is respected. Above the light green curve, the first condition in (31) ($m_{h_2} > m_{h_1}$) is respected. We have $m_s > m_{h_2}$ in the orange region. The points are benchmark points to be presented in Table 2 and Table 3.

4.4 Running couplings from the alignment limit in the IR

Having established the number of independent parameters of the presently considered scenario in the previous subsection, we now consider some further constraints on the (λ_ϕ, μ_3) parameter space and perform the RG analysis of the running couplings.

A necessary requirement for a BSM theory to be phenomenologically viable is that new particle states are heavier than the SM ones if they are strongly coupled to the SM. In the scalar sector of our model, and within the scenario considered thus far, h_2 and s are heavier than the Higgs provided that

$$\begin{cases} \mu_3 > \sqrt{2}\lambda_1 \sin(2\beta) \frac{v^2}{v_\phi}, \\ 2\lambda_\phi v_\phi^2 + \frac{\mu_3}{2\sqrt{2}} \sin(2\beta) \frac{v^2}{v_\phi} > 2\lambda_1 v^2, \end{cases} \quad (31)$$

respectively. On top of that, perturbativity requires, among others, $\lambda_\phi, \lambda_{H\phi}, \lambda_{H'\phi} \leq 4\pi$ and $\mu_3^2 \lesssim 4\pi\bar{m}^2$, where \bar{m} is the heaviest among the physical masses of the scalars h_1, h_2 , and s .

A further restriction on the (λ_ϕ, μ_3) parameter space arises from the stability conditions (17) of the potential. In fact, from the first line in (17), λ_ϕ must be $\lambda_\phi \geq 0$. The other inequalities in (17), (18) are then all trivially respected in this scenario.

The relevant bounds and the hierarchies between physical masses are shown in Fig. 4. In the blue and orange regions, the first condition in (31) ($m_{h_2} > m_{h_1}$) and $m_s > m_{h_2}$ are satisfied, respectively. In the region above the light green curve, the first condition in (31) ($m_{h_2} > m_{h_1}$) is respected. However, $m_s > m_{h_1}$ and $m_s > m_{h_2}$ are not necessary conditions

when the dark Higgs is decoupled from the two doublets. They are rather useful to show the hierarchy between the masses, from which we deduce the relevant unitarity condition as $\mu_3^2 \lesssim 4\pi\bar{m}^2$ where \bar{m}^2 is the heaviest of the three masses. On the contrary, $m_{h_2} > m_{h_1}$ is necessary to get the Higgs couplings consistent with the LHC results and avoid the current LHC bounds on extra scalars in 2HDMs. We indicated with a red dot the benchmark points that will be taken later to analyse the running of the parameters in Table 2 and Table 3.

Performing a numerical investigation of the parameter space, we find as a general feature that the couplings tend to develop a singularity at unacceptably low scales (perturbativity is then clearly lost at lower energies). It is easily understood, comparing to analytic solutions of isolated RGEs for a single coupling, that the singularity encountered by the numerical algorithm is nothing but the Landau pole of the theory (see below for an example of such a comparison). The reason for such low Landau poles is explained below.

Except for λ_1 , the beta functions of the scalar couplings in our model are strongly unbalanced in favour of the bosonic contributions. The IR boundary values of the additional fermion couplings are too small to counterbalance them. For instance, the Yukawa couplings are taken as $y_E = 0.32$ while the IR value of λ_E varies from $\lambda_E = 0.073$ to $\lambda_E = 0.055$ for $v_s = 150$ GeV and $v_s = 200$ GeV, respectively. The IR value of the Z' gauge coupling takes the value $g_{Z'} = 1.15$ and $g_{Z'} = 0.87$ for $v_s = 150$ GeV and $v_s = 200$ GeV, so it is largely the dominant one in the RG equations and rapidly drives the scalar couplings to large values. On top of that, the greater the value of μ_3 , the greater the IR values of $\lambda_{H'\phi}$ and $\lambda_{H\phi}$, so that positive bosonic contributions are even more unbalanced as we take larger values of the cubic coupling μ_3 . In this respect, it is worth to note that the decoupling condition (26) is such that $\lambda_{H'\phi} \sim 30\lambda_{H\phi}$. For the lowest values of μ_3 in agreement with (31) and $\lambda_\phi = 0.1$ (phenomenologically we need even larger values of μ_3 for the additional scalars to be heavy enough), we find a singularity around $\mu = 31$ TeV for $v_s = 150$ GeV and around $\mu = 636$ TeV for $v_s = 200$ GeV.

Table 2 and Table 3 below show the scales where the Landau pole appears and perturbativity is lost for the benchmark points in the left and right plots of Fig. 4, respectively. The way these scales vary in the (λ_ϕ, μ_3) parameter space is easily inferred from the results. As expected, the smaller the values of λ_ϕ and μ_3 , the higher these scales are. However, they do not show a very large sensitivity to changes in the values of λ_ϕ and μ_3 . As already mentioned, the sensitivity to the specific choice of the (λ_3, λ_4) couple is much more suppressed, and is typically beyond the accuracy of our investigation. Nevertheless, it can be seen that among all the possible choices that respect the condition $\lambda_3 + \lambda_4 = 2\lambda_1$ with $\lambda_4 \leq 0$, the one we chose, that is $\lambda_3 = 2\lambda_1$, $\lambda_4 = 0$, is the one with the highest Landau pole.

The two cases considered $v_s = 150$ GeV and $v_s = 200$ GeV correspond to the central value and the highest possible value found in [11] to fit the muon $g - 2$ within 2σ , respectively, but they predict dangerously low scales for Landau pole and perturbativity. As can be easily inferred from a comparison of Table 2 and Table 3, models with larger values of v_s push the problematic scales to slightly higher values. This is mainly due to the fact that $g_{Z'}$ is inversely proportional to v_s . In fact, we will see in next section that the \sim TeV scale Landau pole is mainly generated by the too large IR value of $g_{Z'}$ considered in [11].

Benchmark points in Fig. 4 (Left): $v_\phi = \sqrt{2} \times 150$ GeV								
Point	λ_ϕ	μ_3 (GeV)	Landau pole ($\times 10^4$ GeV)	Perturbativity ($\times 10^3$ GeV)	m_{h_2} (GeV)	m_s (GeV)	$\Delta a_\mu \times$ 10^9	Δm_W (MeV)
A	0.1	19	3.09	10.5	127	98	2.25	70.30
B	0.6	19	2.96	10.2	127	234	2.25	70.30
C	1.1	19	2.73	9.69	127	316	2.25	70.30
D	1.6	19	2.40	9.13	127	380	2.25	70.30
E	0.6	50	2.83	9.55	206	236	2.25	70.30
F	1.1	50	2.60	9.08	206	317	2.25	70.30
G	1.6	50	2.28	8.64	206	382	2.25	70.30
H	2.1	50	1.90	7.92	206	437	2.25	70.30
I	0.6	99	2.61	8.59	290	240	2.25	70.30
L	1.1	99	2.37	8.06	290	320	2.25	70.30
M	1.6	99	2.07	7.55	290	384	2.25	70.30
N	2.1	99	1.73	7.00	290	439	2.25	70.30
O	2.6	99	1.40	6.42	290	487	2.25	70.30

Table 2: Landau pole and perturbativity scales for the benchmark points in the left plot of Fig. 4. The IR value of the couplings λ_3 and λ_4 have been fixed to $(\lambda_3, \lambda_4) = (2\lambda_1, 0)$.

Benchmark points in Fig. 4 (Right): $v_\phi = \sqrt{2} \times 200$ GeV								
Point	λ_ϕ	μ_3 (GeV)	Landau pole ($\times 10^5$ GeV)	Perturbativity ($\times 10^5$ GeV)	m_{h_2} (GeV)	m_s (GeV)	$\Delta a_\mu \times$ 10^9	Δm_W (MeV)
A	0.1	19	6.32	2.22	146	129	1.29	40.64
B	0.6	19	5.37	1.93	146	311	1.29	40.64
C	1.1	19	3.56	1.53	146	420	1.29	40.64
D	1.6	19	1.72	0.870	146	507	1.29	40.64
E	0.6	50	4.81	1.71	238	312	1.29	40.64
F	1.1	50	3.16	1.34	238	421	1.29	40.64
G	1.6	50	1.56	0.79	238	507	1.29	40.64
H	2.1	50	0.616	3.09	238	581	1.29	40.64
I	0.6	100	3.87	1.35	336	314	1.29	40.64
L	1.1	100	2.50	1.04	336	423	1.29	40.64
M	1.6	100	1.28	0.65	336	509	1.29	40.64
N	2.1	100	0.541	0.273	336	582	1.29	40.64
O	2.6	100	0.260	0.131	336	647	1.29	40.64

Table 3: Landau pole and perturbativity scales for benchmark points in the right plot of Fig. 4. The same choice has been made for λ_3 and λ_4 .

More generally, in the following subsections we will systematically address issues found that will present themselves in the RG analysis of the benchmark points. This will drive us to a different and somehow restricted region of the parameter space.

4.5 Z' mass dependence of the Landau pole

We advanced in the previous section that the major architect of the low Landau pole is the large IR value of $g_{Z'}$. The study of the RGEs with $m_{Z'} < 500$ GeV, that correspond to lower values of $g_{Z'}$, confirms this expectation. For instance, taking the parameters given in point A for $v_s = 200$ GeV and $m_{Z'} = 250$ GeV, one finds a singularity at 7.89×10^{13} GeV: reducing $m_{Z'}$ by a factor 1/2 pushes the singularity (and with it, the perturbativity scale) 8 order of magnitudes forward. Other representative cases are collected in Table 3, where it is seen that, for $v_s = 200$ GeV and $\lambda_\phi = 0.1$, the Landau pole can be brought around the Planck scale by taking $m_{Z'} = 200$ GeV. For $v_s = 150$ GeV and $\lambda_\phi = 0.4$, a scenario that is of greater interest in light of the results shown in Fig. 1 and of the values of the masses reported in Table 2 and Table 3, a Planck scale Landau pole cannot be obtained: further decreases of $m_{Z'}$ do not make any improvement on the results displayed for $m_{Z'} = 200$ GeV. We will try in the following to relax some assumptions on the scalar couplings to further increase the pole scale while still fitting the experimental anomalies. We note that besides the above theoretical remarks, values for $m_{Z'}$ smaller than 250 GeV are phenomenologically disfavored by the direct Z' searches at the LHC, as discussed in Section 3, and we will not consider them.

Concerning the decrease of the IR value of $m_{Z'}$, it should be noted that the solution to the W boson mass anomaly presented in [11], that, as recalled above, is based on a tree-level correction to the W self-energy due to the Z - Z' mixing, requires $m_{Z'}$ to be sufficiently larger than m_Z . In this case, in fact, BSM physics brings in a positive correction to the mass, and a region of parameter space where the CDF II measurement can be explained within 1σ was found [11]. On the contrary, in the opposite limit $m_{Z'} \ll m_Z$, the contribution to the W boson mass from BSM physics is negative. Clearly, the findings from CDF II cannot be accommodated with the inverted hierarchy. As can be seen in Table 4₁ (see also Fig. 1, where a different value for λ_ϕ was taken), the correction Δa_μ to the muon $g - 2$ and the correction Δm_W to the W boson mass are still of the right order to fit the experimental anomalies for $m_{Z'} \gtrsim 250$ GeV, i.e. for values of $m_{Z'}$ in agreement with LHC searches for additional Z bosons and below which the Landau pole does not sensibly increase any more.

A more quantitative estimate of the role of $g_{Z'}$ in generating the low scale Landau pole can be obtained taking the RGE for $g_{Z'}$,

$$\mu \frac{d}{d\mu} g_{Z'}(\mu) = \frac{7}{12\pi^2} g_{Z'}^3(\mu) \quad \longrightarrow \quad g_{Z'} = \frac{1}{\sqrt{\frac{1}{g_{Z'}^2(\mu_{\text{IR}})} - \frac{7}{6\pi^2} \log\left(\frac{\mu}{\mu_{\text{IR}}}\right)}}, \quad (32)$$

and calculating its Landau pole $\mu_L = \mu_{\text{IR}} e^{6\pi^2/7g_{Z'}^2(\mu_{\text{IR}})}$ for the different IR values of $g_{Z'}$ in the two sets of the parameters in Table 4. The Landau pole of the full model is compared to μ_L

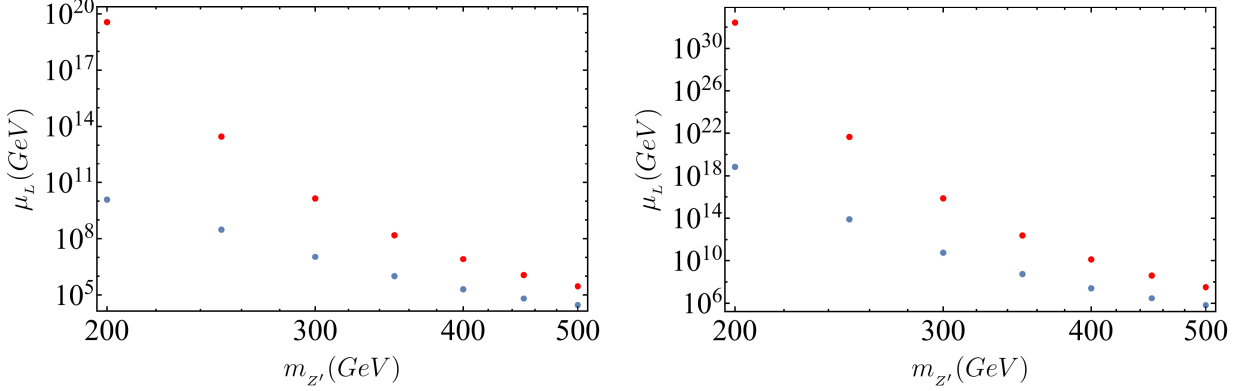


Figure 5: The blue points indicate the Landau pole of the full model, the red ones the Landau pole of Eq. (32) for two sets of parameters in Table 4: the upper table for the left panel and the lower table for the right panel.

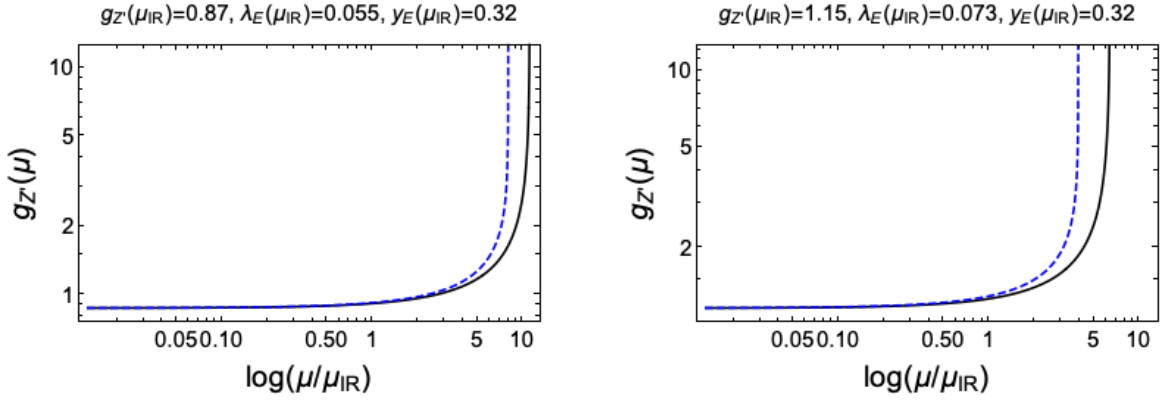


Figure 6: Running $g_{z'}$ coupling at one-loop and two-loop levels, in black solid and blue dashed lines, respectively. We considered two benchmark models with $(g_{z'}, \lambda_E, y_E) = (0.87, 0.055, 0.32)$ and $(1.15, 0.073, 0.32)$, on the left and right plots, respectively.

in Fig. 5, where it can be seen that the higher the value of $m_{z'}$ ($g_{z'}$), the closer the two are. It is easy to conclude from this plot that, for “high enough” (IR) values of $g_{z'}$, the Landau pole is almost fully determined by the gauge coupling, that, through its contribution in their beta functions, causes the other couplings to diverge at slightly lower values. Lowering the (IR) value of $g_{z'}$, the Landau pole of (32) becomes considerably higher than that of the full model. In this region of parameter space, the appearance of the Landau pole is a more “collective” phenomenon. All the couplings conspire together to generate it, and the determination of the pole scale from the RG equation of $g_{z'}$ taken in isolation does not provide a good approximation to the pole scale of the full model any more.

It is worthwhile to make comments on the effects of two-loop corrections in view of the low scale Landau pole, although a complete two-loop analysis in our model is beyond the scope of our current work. The RG equation for the extra gauge coupling at the two-loop

level [34] is given by

$$\mu \frac{d}{d\mu} g_{z'}(\mu) = \frac{7}{12\pi^2} g_{z'}^3 + \frac{1}{(4\pi)^4} \left(256g_{z'}^5 - 16g_{z'}^3 (\lambda_E^2 + 2y_E^2) \right). \quad (33)$$

Then, ignoring the running of the extra Yukawa couplings, λ_E and y_E , we get the approximate solution for the running extra gauge coupling at two-loops as

$$g_{z'}(\mu) \simeq \left[\frac{1}{g_{z'}^2(\mu_{\text{IR}})} - \frac{98 \log\left(\frac{\mu}{\mu_{\text{IR}}}\right)}{3(28\pi^2 + 3\lambda_E^2 + 6y_E^2)} - \frac{96 \log\left(\frac{g_{z'}(\mu)}{g_{z'}(\mu_{\text{IR}})}\right)}{28\pi^2 + 3\lambda_E^2 + 6y_E^2} \right]^{-1/2}. \quad (34)$$

Then, we get the Landau pole modified to

$$\mu_L \simeq \mu_{\text{IR}} \exp \left[\frac{6\pi^2}{7g_{z'}^2(\mu_{\text{IR}})} \left(1 + \frac{3\lambda_E^2}{28\pi^2} + \frac{3y_E^2}{14\pi^2} \right) - \frac{144}{49} \log\left(\frac{g_{z'}(\mu_L)}{g_{z'}(\mu_{\text{IR}})}\right) \right]. \quad (35)$$

Here, we can take the extra gauge coupling at the Landau pole in the correction term as $g_{z'}(\mu_L) = 4\pi$ for which perturbativity breaks down. For instance, for $\lambda_E = 0.055 - 0.073$ and $y_E = 0.32$ in our benchmark models in Section 4.3, we find that the scale of the Landau pole gets reduced sizably at two-loop order due to the two-loop gauge interactions, as compared to the one-loop results. In the left and right plots in Fig. 6, we also depict the running $g_{z'}$ for the same benchmark models by the numerical analysis at one-loop and two-loop levels, in black solid and blue dashed lines, respectively. As a result, we find that the two-loop corrections are minor far away from the Landau pole, but they become important near the Landau pole. However, the very existence of the Landau pole at a low scale can be identified by the one-loop results, indicating the violation of perturbativity, so we can rely on the one-loop corrections in our RG analysis to extract the meaningful information on the Landau pole. Similar conclusions can be drawn for the perturbativity and stability of the other running couplings such as the Higgs quartic couplings in our model, but we postpone the detailed analysis with two-loop corrections to another work.

When the pole scale is increased above $\sim 10^8$ GeV, the range of the flow is large enough to see the appearance of an instability of the scalar potential. As in the SM, this is due to the fact that the Higgs-like quartic coupling $\lambda_1(\mu)$ becomes negative while running toward high energies⁷. The scale where such an instability appears is indicated for some representative cases in Table 4. This should be compared to the corresponding case of the SM, where, with our parametrization, $\lambda(\mu) = 0$ for $\mu \sim 1.48 \times 10^8$ GeV at the one-loop level⁸. The shift in the IR boundary value of the top coupling caused by the $\cos\beta$ factor in $m_t = y_t v \cos\beta/\sqrt{2}$ competes with the presence of several additional bosonic states in such a way that, with the IR boundary values chosen in Table 4, the instability scale does not change much with respect to the SM one.

In Fig. 7, a comparison between the flow of $\lambda_1(\mu)$ in our model and the flow of $\lambda(\mu)$ in the SM can be found for $v_s = 200$ GeV, $\lambda_\phi = 0.1$, $\mu_3 = 19$ GeV and $m_{z'} = 300$ GeV (left panel),

⁷The other stability conditions (17), (18) are respected with the running couplings for all (admissible) values of μ .

⁸With our parametrization, the SM quartic coupling vanishes for $\mu \sim 1.25 \times 10^{10}$ GeV at the two-loops.

Parameter set: $v_\phi = \sqrt{2} \times 150$ GeV, $\lambda_\phi = 0.4$, $\mu_3 = 50$ GeV, $\sin \beta = 0.18$					
$m_{Z'}(\text{GeV}) \rightarrow g_{Z'}$	LP (GeV)	Pert (GeV)	VSB (GeV)	$\Delta a_\mu \times 10^9$	$\Delta m_W(\text{MeV})$
500 \rightarrow 1.15	2.90×10^4	9.71×10^3	–	2.25	70.30
450 \rightarrow 1.04	6.51×10^4	2.18×10^4	–	2.15	70.25
400 \rightarrow 0.92	2.02×10^5	6.86×10^4	–	2.06	70.17
350 \rightarrow 0.81	1.02×10^6	3.59×10^5	–	1.97	70.01
300 \rightarrow 0.69	1.09×10^7	4.07×10^6	–	1.88	69.66
250 \rightarrow 0.58	3.05×10^8	1.36×10^8	–	1.80	68.75
200 \rightarrow 0.46	1.22×10^{10}	7.83×10^9	2.50×10^8	1.72	68.61

Parameter set: $v_\phi = \sqrt{2} \times 200$ GeV, $\lambda_\phi = 0.1$, $\mu_3 = 19$ GeV, $\sin \beta = 0.18$					
$m_{Z'}(\text{GeV}) \rightarrow g_{Z'}$	LP (GeV)	Pert (GeV)	VSB (GeV)	$\Delta a_\mu \times 10^9$	$\Delta m_W(\text{MeV})$
500 \rightarrow 0.87	6.32×10^5	2.22×10^5	–	1.29	40.64
450 \rightarrow 0.79	2.91×10^6	1.04×10^6	–	1.23	40.61
400 \rightarrow 0.70	2.46×10^7	9.15×10^6	–	1.18	40.56
350 \rightarrow 0.61	5.32×10^8	2.08×10^8	1.35×10^8	1.13	40.47
300 \rightarrow 0.52	5.30×10^{10}	2.23×10^{10}	1.19×10^8	1.08	40.27
250 \rightarrow 0.44	6.43×10^{13}	3.10×10^{13}	1.59×10^8	1.03	39.75
200 \rightarrow 0.35	3.08×10^{18}	1.82×10^{18}	2.49×10^8	0.99	37.94

Table 4: Landau pole (LP), Perturbativity (Pert) and Vacuum stability (VSB) scales for some Z' masses with two examples for the parameter set. In the last two columns, we also showed the numerical values of the corrections to the muon $g - 2$ and the W boson mass in our model.

$m_{Z'} = 200$ GeV (right panel). This choice of parameters allow to have a larger domain for the the RG evolution. The behaviour of $\lambda_1(\mu)$ just discussed goes against the naive expectation that the presence of (several) additional bosonic states automatically improves stability; there is rather a delicate competition between the enhanced top quark contribution and the BSM ones. As we will see below, radiative stability of the potential can be realized, but the positive shift in the top coupling caused by the enlargement of the scalar sector makes it a not too trivial matter. It should also be noted that, thanks to the additional bosonic degrees of freedom, after crossing zero $\lambda_1(\mu)$ soon stops its descent and starts to grow faster than in the SM. In the case depicted in Fig. 7₂, for instance, the coupling becomes positive again for $\mu \gtrsim 10^{16}$ GeV before reaching its Landau pole at $\mu \sim 3 \times 10^{18}$ GeV.

5 General alignment limits in the IR

We extend the RG analysis to the cases where the doublets are not completely decoupled from the scalar singlet, and their quartic couplings do not necessarily realize alignment.

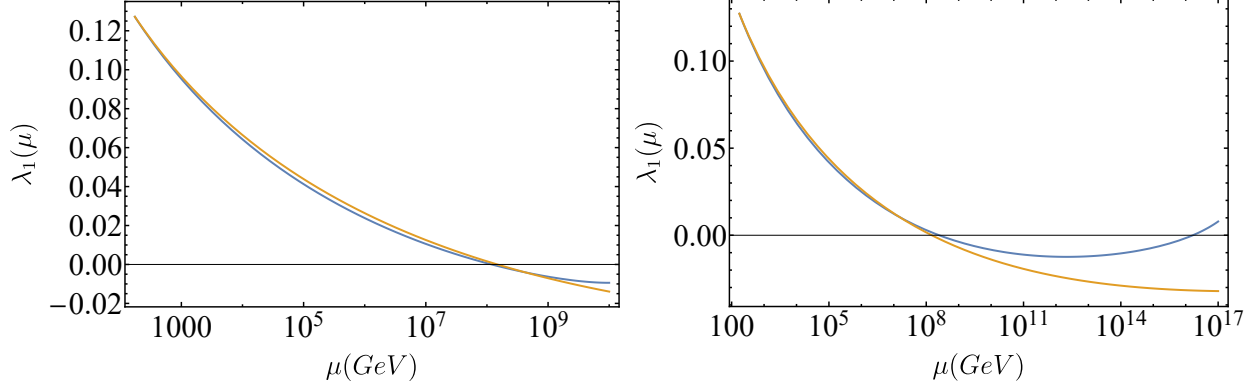


Figure 7: The blue curve indicates the flow of λ_1 for the choice of parameters corresponding to point A in Table 3 and with $m_{z'} = 300$ GeV (left panel) $m_{z'} = 200$ GeV (right panel). The yellow curve corresponds to the flow of λ_1 in the Standard Model.

5.1 Detuning quartic couplings

So far, we followed [11] in the determination of the conditions for alignment. Namely, we took the condition $\lambda_1 = \lambda_2 = \lambda_{34}/2$ for the IR parameters that, as stressed above, was shown in [35] to correspond to the maximally symmetric configuration for the scale-invariant sector of the classical potential $V(\phi, H, H')$ in (4). As already observed in [11], however, this is only a particular solution that realizes the alignment of the two Higgs doublets. Below, we derive the general solution for alignment imposing as a constraint that the lowest eigenvalue of the 2×2 mass matrix $\widetilde{\mathcal{M}}_H^2$ (28) coincides with the physical Higgs boson mass.

Taking $\widetilde{\mathcal{M}}_H^2$, that we rewrite here for the ease of the reader,

$$\widetilde{\mathcal{M}}_H^2 = \begin{pmatrix} 2\lambda_1 v_1^2 + \frac{\mu_3}{\sqrt{2}} \tan \beta v_\phi & \lambda_{34} v_1 v_2 - \frac{\mu_3}{\sqrt{2}} v_\phi \\ \lambda_{34} v_1 v_2 - \frac{\mu_3}{\sqrt{2}} v_\phi & 2\lambda_2 v_2^2 + \frac{\mu_3}{\sqrt{2}} \cot \beta v_\phi \end{pmatrix},$$

and applying a rotation of angle β parametrized by the matrix S_β , we obtain

$$\widetilde{\mathcal{M}}_{H,\beta}^2 \equiv S_\beta^{-1} \widetilde{\mathcal{M}}_H^2 S_\beta = \begin{pmatrix} A & C \\ C & B \end{pmatrix}, \quad (36)$$

with

$$A = 2 (\lambda_1 \cos^4 \beta + \lambda_{34} \cos^2 \beta \sin^2 \beta + \lambda_2 \sin^4 \beta) v^2, \quad (37)$$

$$B = \frac{1}{\sqrt{2}} \frac{\mu_3 v_\phi}{\sin \beta \cos \beta} + 2 \sin^2 \beta \cos^2 \beta (\lambda_1 + \lambda_2 - \lambda_{34}) v^2, \quad (38)$$

$$C = ((\lambda_{34} - 2\lambda_1) \cos^3 \beta \sin \beta + (2\lambda_2 - \lambda_{34}) \sin^3 \beta \cos \beta) v^2. \quad (39)$$

In the following, we denote with h and h' the two mass eigenstates obtained after diagonalization:

$$\begin{pmatrix} h \\ h' \end{pmatrix} = S_\beta^{-1} \begin{pmatrix} h_1 \\ h_2 \end{pmatrix}. \quad (40)$$

In terms of λ_{34} , the general solution to the equation $C = 0$ reads

$$\lambda_{34} = 2 \frac{\lambda_1 - \lambda_2 \tan^2 \beta}{1 - \tan^2 \beta}. \quad (41)$$

For later convenience, it is useful to also solve (41) in terms of $\tan \beta$ as (this is only well defined when $2\lambda_2 - \lambda_{34} \neq 0$)

$$\tan^2 \beta = \frac{2\lambda_1 - \lambda_{34}}{2\lambda_2 - \lambda_{34}}. \quad (42)$$

Moreover, for A to be the SM Higgs squared mass $m_h^2 = 2\lambda_{\text{SM}}v^2$, we need⁹ $\lambda_1 \cos^4 \beta + \lambda_3 \cos^2 \beta \sin^2 \beta + \lambda_2 \sin^4 \beta = \lambda_{\text{SM}}$, where λ_{SM} is the Standard Model Higgs quartic coupling. In passing, we note that this condition also guarantees that the three and four point vertices for the Higgs boson h obtained after diagonalization are the same as in the SM. Solving for λ_2 , we get

$$\lambda_2 = \lambda_1 + (\lambda_1 - \lambda_{\text{SM}}) \frac{\cos 2\beta}{\sin^4 \beta}. \quad (44)$$

Finally, inserting (44) in (41), the latter becomes

$$\lambda_{34} = 2\lambda_1 - 2 \frac{\lambda_1 - \lambda_{\text{SM}}}{\sin^2 \beta}. \quad (45)$$

These last equations are quite interesting, as they tell us how much a detuning of λ_1 from λ_{SM} affects λ_2 and λ_{34} if we keep the SM Higgs in the alignment limit. It is immediate to realize that, for small β (as required by the W boson mass as well as LHC bounds), the coefficient $\cos 2\beta/\sin^4 \beta$ in front of $\lambda_1 - \lambda_{\text{SM}}$ in (44) (the coefficient $1/\sin^2 \beta$ as well, although it is obviously smaller) is very large. For instance, for $\sin \beta = 0.18$ we have $\cos 2\beta/\sin^4 \beta \sim 891$ and $1/\sin^2 \beta \sim 31$. Needless to say, “large” values of the scalar couplings are unacceptable, as they easily result in too low Landau pole scales. For instance, a 0.47% relative detuning of λ_1 with respect to the last example shown in Table 4₂, $\lambda_1 - \lambda_{\text{SM}} = 0.0006$ (we take $\lambda_{\text{SM}} = 0.1272$ at the top scale m_t), results in a 421% relative detuning of λ_2 , $\lambda_2 - \lambda_{\text{SM}} = 0.54$, a 14% relative detuning of λ_{34} , $\lambda_{34} - 2\lambda_{\text{SM}} = -0.04$, and brings the Landau pole down from $\mu_L \sim 3 \times 10^{18}$ GeV to $\mu_L \sim 7 \times 10^7$ GeV.

The extreme sensitivity of the couplings, especially of λ_2 , to the detuning of λ_1 from λ_{SM} tells us that the constraint brought by eq. (44) is extremely tight. Detuning λ_1 to larger values $\lambda_1 > \lambda_{\text{SM}}$ might stabilize the vacuum, but we see here that it does not come without cost. For benchmark points as the last one in Table 4₁, one can devise a small enough detuning to shift the $\lambda_1(\mu)$ curve all in the upper half plane up to a Landau pole that is sufficiently far from the SM (one-loop) instability scale $\mu \sim 10^8$ GeV, making the indication of one-loop vacuum stability quite trustable. However, the same cannot be done

⁹For consistency, this should be accompanied by

$$\frac{\mu_3 v_\phi}{\sqrt{2} \sin \beta \cos \beta} \geq \left(\lambda_1 + \lambda_2 + \frac{\lambda_1 - \lambda_2}{\cos 2\beta} \right), \quad (43)$$

otherwise the second Higgs boson h' is lighter than the SM Higgs.

for benchmarks of phenomenological interest, such as the $m_{z'} \gtrsim 250$ GeV ones in Table 4₂. There is in fact too little a hierarchy between the Landau pole in the tuned scenario and the instability scale (when it exists) to shift the couplings and obtain truthful indications for stability.

Before closing this section, we should note that (44), as well as a slight generalization of (45), is not restricted to the present model, but is of more general validity for 2-Higgs doublet models. In $\widetilde{\mathcal{M}}_S^2$, in fact, the dark Higgs field ϕ only accounts for the presence of μ_3 , from which A and C are independent. More precisely, after a \mathbb{Z}_2 symmetry $H_1 \rightarrow H_1$, $H_2 \rightarrow -H_2$ is imposed and a real small breaking parameter μ_{12} is inserted, the inert 2-Higgs doublet model's potential reads

$$V = \mu_1^2 |H_1|^2 + \mu_2 |H_2|^2 - \mu_{12}^2 \left(H_1^\dagger H_2 + \text{h.c.} \right) + \lambda_1 |H_1|^4 + \lambda_2 |H_2|^4 + \lambda_3 |H_1|^2 |H_2|^2 + \lambda_4 |H_1^\dagger H_2|^2 + \frac{\lambda_5}{2} \left((H_1^\dagger H_2)^2 + (H_2^\dagger H_1)^2 \right). \quad (46)$$

Using the minimization conditions, that for a normal vacuum

$$H_1 = \frac{1}{\sqrt{2}} \begin{pmatrix} 0 \\ v_1 \end{pmatrix}, \quad H_2 = \frac{1}{\sqrt{2}} \begin{pmatrix} 0 \\ v_2 \end{pmatrix} \quad (47)$$

with $v_2/v_1 = \tan \beta$, amount to

$$\begin{cases} \mu_1^2 + \lambda_1 v_1^2 + \frac{\lambda_3 + \lambda_4 + \lambda_5}{2} v_2^2 = \mu_{12}^2 \frac{v_2}{v_1}, \\ \mu_2^2 + \lambda_2 v_2^2 + \frac{\lambda_3 + \lambda_4 + \lambda_5}{2} v_1^2 = \mu_{12}^2 \frac{v_1}{v_2}, \end{cases} \quad (48)$$

and defining $\lambda_{345} \equiv \lambda_3 + \lambda_4 + \lambda_5$, the neutral CP-even mass matrix reads, in the vacuum,

$$\mathcal{M}^2 = \begin{pmatrix} 2\lambda_1 v_1^2 + \mu_{12}^2 \tan \beta & \lambda_{345} v^2 \sin \beta \cos \beta - \mu_{12}^2 \\ \lambda_{345} v^2 \sin \beta \cos \beta - \mu_{12}^2 & 2\lambda_2 v_2^2 + \mu_{12}^2 \cot \beta \end{pmatrix}.$$

The above matrix is the same as $\widetilde{\mathcal{M}}_S^2$ in (28) with $\mu_3 v_\phi / \sqrt{2}$ replaced by μ_{12}^2 and λ_{34} replaced by λ_{345} . A rotation by an angle β would then produce the same matrix as (36), with replacements in A , B and C similar to those discussed above. The equations $A = 2\lambda_{\text{SM}} v^2$ and $C = 0$ then result in the conditions

$$\begin{cases} \lambda_{345} = 2\lambda_1 - 2 \frac{\lambda_1 - \lambda_{\text{SM}}}{\sin^2 \beta} \\ \lambda_2 = \lambda_1 + (\lambda_1 - \lambda_{\text{SM}}) \frac{\cos 2\beta}{\sin^4 \beta}, \end{cases} \quad (49)$$

that provide only a slight generalization to (44) and (45). The consequences, of course, are the same.

5.2 General decoupling of the singlet scalar

Acceptable values of the additional bosons' physical masses are obtained only with sufficiently large values of μ_3 . As $\cot \beta \sim 5.5$, large values of μ_3 can easily result in dangerously large IR values for $\lambda_{H'\phi}$.

The decoupling scenario of [11], where the scalar field s is decoupled from h_1 and h_2 , can actually be relaxed to a more general scenario, within which large values of μ_3 can be more easily accommodated, and the Landau poles found for $v_s = 150$ GeV can be slightly uplifted. Taking the 3×3 scalar mass matrix \mathcal{M}_H^2 (A.5) in the vacuum, in fact, we can first diagonalize its 2×2 upper part ($\widetilde{\mathcal{M}}_H^2$), which results in the change of basis $(h_1, h_2) \rightarrow (h, h')$, and then require the scalar s to be decoupled from the physical Higgs boson h . Borrowing the notation of Appendix A for the components of \mathcal{M}_H^2 , after a rotation of angle α in the (h_1, h_2) subspace the mass matrix \mathcal{M}_H^2 reads

$$\mathcal{M}_H^2 = \begin{pmatrix} A & B & C \\ B & D & E \\ C & E & F \end{pmatrix}, \quad (50)$$

with

$$A = \frac{1}{2} (M_{H,11}^2 + M_{H,22}^2 + (M_{H,11}^2 - M_{H,22}^2) \cos 2\alpha + 2M_{H,12}^2 \sin 2\alpha), \quad (51)$$

$$B = \frac{1}{2} (M_{H,22}^2 - M_{H,11}^2) \sin 2\alpha + M_{H,12}^2 \cos 2\alpha, \quad (52)$$

$$C = M_{H,13}^2 \cos \alpha + M_{H,23}^2 \sin \alpha, \quad (53)$$

$$D = \frac{1}{2} (M_{H,11}^2 + M_{H,22}^2 - (M_{H,11}^2 - M_{H,22}^2) \cos 2\alpha - 2M_{H,12}^2 \sin 2\alpha), \quad (54)$$

$$E = M_{H,23}^2 \cos \alpha - M_{H,13}^2 \sin \alpha, \quad (55)$$

$$F = M_{H,33}^2. \quad (56)$$

As it is well-known, the diagonalization condition $B = 0$ reads

$$\tan 2\alpha = -2 \frac{M_{H,12}^2}{M_{H,22}^2 - M_{H,11}^2}, \quad (57)$$

and A must be $A = m_h^2$, with m_h the Higgs mass. Decoupling the Higgs h from s amounts to require

$$M_{H,13}^2 \cos \alpha + M_{H,23}^2 \sin \alpha = 0. \quad (58)$$

Plugging the explicit expressions of $M_{H,13}^2$ (A.9) and $M_{H,23}^2$ (A.10) in (58), we obtain

$$(\lambda_{H\phi} \cos \alpha \cos \beta + \lambda_{H'\phi} \sin \alpha \sin \beta) v_\phi = \frac{\mu_3}{\sqrt{2}} (\cos \alpha \sin \beta + \sin \alpha \cos \beta). \quad (59)$$

In the alignment limit $\alpha = \beta$, the above expression simplifies to

$$(\lambda_{H\phi} \cos^2 \beta + \lambda_{H'\phi} \sin^2 \beta) v_\phi = \sqrt{2} \mu_3 \sin \beta \cos \beta. \quad (60)$$

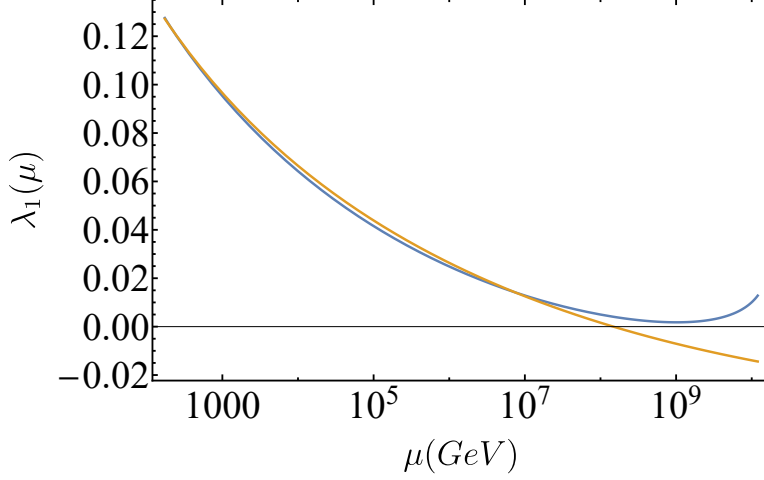


Figure 8: Comparison between the the flow of $\lambda_1(\mu)$ (blue curve) and the flow of $\lambda(\mu)$ in the Standard Model (yellow curve) for the benchmark point with $m_{z'} = 250$ GeV in Table 4₁ in the detuned scenario with IR boundary values $\lambda_1 = 0.12746$, $\lambda_4 = 0$, $\lambda_{H'\phi} = -2\sqrt{\lambda_2\lambda_\phi} \sim -0.758$, $\lambda_{H\phi} = \sqrt{2}\frac{\mu_3 \tan\beta}{v_\phi} - \lambda_{H'\phi} \tan^2\beta \sim 0.086$ and λ_2, λ_3 determined from (44) and (45), respectively.

It is immediate to verify that $\lambda_{H\phi} = \mu_3 \tan\beta/(\sqrt{2}v_\phi)$ and $\lambda_{H'\phi} = \mu_3 \cot\beta/(\sqrt{2}v_\phi)$ give a specific solution of (60) that also realize $E = 0$, as it should.

With the conditions above, the “semi-diagonalized” matrix becomes

$$\begin{pmatrix} \lambda^- & 0 & 0 \\ 0 & \lambda^+ & \frac{M_{H,23}^2}{\cos\alpha} \\ 0 & \frac{M_{H,23}^2}{\cos\alpha} & M_{H,33}^2 \end{pmatrix}, \quad (61)$$

with

$$\lambda^\pm = \frac{1}{2} \left(M_{H,11}^2 + M_{H,22}^2 \pm (M_{H,22}^2 - M_{H,11}^2) \sqrt{\frac{(M_{H,22}^2 - M_{H,11}^2)^2 + 4M_{H,12}^4}{(M_{H,22}^2 - M_{H,11}^2)^2}} \right). \quad (62)$$

As we want the Higgs to be the lightest scalar, we also require $\lambda^- < \lambda^+$. This is satisfied when $M_{H,22}^2 > M_{H,11}^2$, in which case the above expressions for λ^\pm easily simplify. Finally, the eigenvalues of the 2×2 lower mass matrix will give the physical masses of the additional scalars as

$$m_\pm^2 = \frac{1}{2} \left(\lambda^+ + M_{H,33}^2 \pm \sqrt{(\lambda^+ - M_{H,33}^2)^2 + 4\frac{M_{H,23}^4}{\cos^2\alpha}} \right). \quad (63)$$

Using the general solution for decoupling described in this section, we can now study the RG flow of the parameters from the benchmark point with $m_{z'} = 250$ GeV in Table 4₁ as we take different solutions of eq. (60) for $\lambda_{H\phi}$ and $\lambda_{H'\phi}$. The numerical investigation indicate that higher values for the Landau pole are obtained for higher values of $\lambda_{H\phi}$. In particular, the highest possible value is found combining eq. (60) with the stability conditions (17),

(18), in particular saturating the inequality $\lambda_{H'\phi} + 2\sqrt{\lambda_2\lambda_\phi} \geq 0$. For the $(\lambda_{H\phi}, \lambda_{H'\phi})$ couple determined in this way, we find $\mu_L \sim 2.18 \times 10^9$ GeV and an instability scale $\mu_i \sim 1.03 \times 10^8$ GeV for $\lambda_1 = \lambda_{\text{SM}}$. A detuning of λ_1 then allows to find points that generate Landau pole scales $\mu_L \lesssim 10^9$ GeV and a one-loop stable potential up to μ_L . For instance, we find $\mu_L \sim 9.69 \times 10^8$ GeV, with a perturbativity scale $\mu_P \sim 5.47 \times 10^8$ GeV, and the flow reported in Fig. 8 for a 0.2% detuning of λ_1 ($\lambda_1 = 0.12746$). Another convenient choice for $\lambda_{H\phi}$ and $\lambda_{H'\phi}$ might be $\lambda_{H\phi} = \lambda_{H'\phi}$, for which we find $\mu_L \sim 1.33 \times 10^9$ GeV in the tuned scenario ($\lambda_1 = \lambda_{\text{SM}}$). The differences between the two cases are too small to be considered as significant ones within our one-loop investigation, whose aim is rather to assess the viability of our model with respect to its flow towards the UV, to find the approximate scale at which new physics should complete it, and understand whether it can lead to a (more) stable potential or not. We will see, in the next section, that the second choice is actually more interesting as it will leave us more freedom to explore the parameter space of the theory when the two doublets are not aligned.

5.3 Breaking the alignment

We comment in this section on the possibility of relaxing the assumption that the two doublets are in the aligned limit. We consider, instead, the (h_1, h_2) mass matrix $\widetilde{\mathcal{M}}_H^2$ to be diagonalized by a generic angle in the vacuum.

To this end, we perform, as in Section 5.2, a rotation of angle α in the (h_1, h_2) subspace, and impose the following conditions: (i) the resulting matrix is diagonal in its 2×2 upper left component, that is $B = 0$ in (52); (ii) the resulting Higgs field h is decoupled from the dark Higgs, that is $C = 0$ in (55); and (iii) the $(1, 1)$ component of the matrix obtained after diagonalization is equal to m_h^2 , that is $A = m_h^2$ in (51). The second condition simply gives eq. (59). The other two conditions can be solved for λ_2 and λ_{34} , for instance, and give

$$\lambda_2 = \lambda_1 \frac{\sin^2 \alpha - \cos^2 \alpha \sin^2 \beta}{\sin^2 \alpha \sin^2 \beta} + (\lambda_1 - \lambda_{\text{SM}}) \frac{\cos 2\alpha}{\sin^2 \alpha \sin^2 \beta} + \frac{\mu_3 v_\phi}{4v^2} \frac{\cos 2\alpha - \cos 2\beta}{\sin^2 \alpha \sin^3 \beta \cos \beta}, \quad (64)$$

$$\lambda_{34} = -\frac{2v^2 \cot \alpha (\lambda_1 - \lambda_{\text{SM}} - \lambda_1 \sin^2 \beta) + \mu_3 v_\phi (\cot \alpha \tan \beta - 1)}{v^2 \sin \beta \cos \beta}. \quad (65)$$

It is immediate to verify that the two equations above reduce to (44) and (45), respectively, when $\alpha = \beta$. Equations (64) and (65) show an interesting interplay between the quartic coupling λ_1 and the diagonalization angle α . As we will see, a misalignment in the doublets can be used to tame the enhancement found in (44) and (45) for detuned quartic couplings $\lambda_1 \neq \lambda_{\text{SM}}$.

Fixing all the other couplings to the convenient values (and/or expressions) found in the previous sections, the only two free parameters are λ_1 and α . The two-dimensional space they span is restricted by theoretical and phenomenological requirements. Specifically, we impose the tree-level stability conditions (17) and (18), perturbativity of the couplings, positiveness of the eigenvalues (63) and an upper bound on the misalignment, namely $\sin^2(\alpha - \beta) \leq 0.1$, for the latter to be consistent with observations (the precise value of the upper bound is

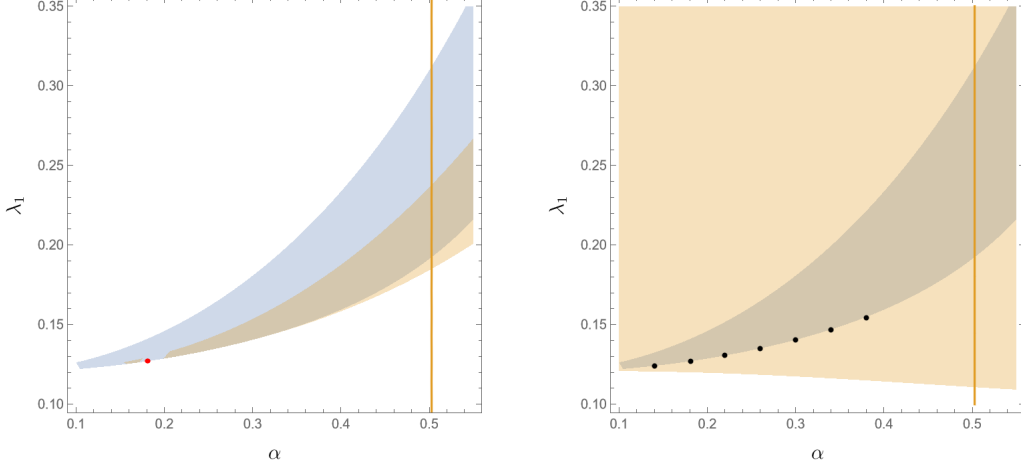


Figure 9: Two-dimensional section of the parameter space. *Left panel:* All the couplings other than α and λ_1 are fixed to the values and/or expressions described in the text (in particular, $v_s = 150$ GeV, $\mu_3 = 50$ GeV, $m_{Z'} = 250$ GeV and $\lambda_\phi = 0.4$, as in Table 4₁). In the blue region, tree-level stability and perturbativity of the couplings are realized. In the yellow region, the lowest eigenvalue m_-^2 in (63) is positive. Numerical complications arise when it becomes thinner. The yellow line corresponds to $\sin^2(\alpha - \beta) = 0.1$. The red dot indicates the point of coordinates $(\alpha, \lambda_1) = (\beta, \lambda_{\text{SM}})$. *Right panel:* Same plot as in the left panel, the only difference being the choice for $\lambda_{H\phi}$ and $\lambda_{H'\phi}$, that here are taken as the solution with $\lambda_{H\phi} = \lambda_{H'\phi}$. The black dots indicate the benchmark points in Table 5.

unimportant and was chosen arbitrarily; it only amounts to a shift of the yellow line in the plots shown in Fig. 9). The resulting parameter space is shown in Fig. 9 (blue region). The only couplings, other than λ_2 and λ_{34} , that depend on λ_1 and α when adopting the procedure outlined above are $\lambda_{H'\phi}$ and $\lambda_{H\phi}$, either through the choice $\lambda_{H'\phi} = -2\sqrt{\lambda_2\lambda_\phi}$ in combination with eq. (59), or through the choice

$$\lambda_{H\phi} = \lambda_{H'\phi} = \frac{\mu_3}{\sqrt{2}v_\phi} \frac{\sin(\alpha + \beta)}{\cos(\alpha - \beta)}. \quad (66)$$

In both cases, the stability and perturbativity constraints on these couplings are milder than those on λ_2 and λ_{34} . Nevertheless, the difference between the left panel and the right panel in Fig. 9 shows an extreme sensitivity of the sign of m_-^2 in (63) on the specific choice of the couple $(\lambda_{H\phi}, \lambda_{H'\phi})$ that solves (59). In the left plot, in fact, the choice $\lambda_{H'\phi} = -2\sqrt{\lambda_2\lambda_\phi}$ leads to a strong constraint on the allowed region of parameter space. In this case, the point $(\lambda = \lambda_{\text{SM}}, \alpha = \beta)$ that represents the tuned and aligned scenario is in a tiny allowed region around which numerical complications arise that make the plot discontinuous. To be certain that this feature is only a result of numerical difficulties, we checked, for several points nearby that are not coloured in yellow, that they correctly have $m_-^2 > 0$. In the right plot, the choice $\lambda_{H\phi} = \lambda_{H'\phi}$ is shown to leave much more freedom to move in the parameter space, as the blue region is entirely contained in the yellow one. Physically, this means that no constraint arises from the condition $m_-^2 \geq 0$ in eq. (63).

Given the above considerations, we can conclude that, unless specific choices for $\lambda_{H\phi}(\alpha, \lambda_1)$ and $\lambda_{H'\phi}(\alpha, \lambda_1)$ that make their dependence on α and λ_1 strongly constraining are made, the

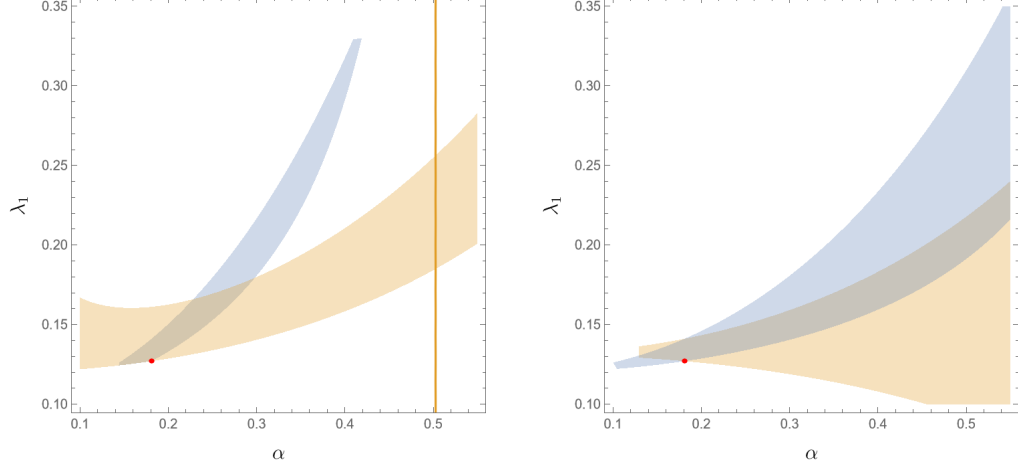


Figure 10: *Left panel:* Same plot as in the left panel of Fig. 9 for a different choice of μ_3 and v_ϕ , namely $\mu_3 = 380$ GeV and $v_s = 250$ GeV. The red dot again indicates the point $\alpha = \beta$, $\lambda = \lambda_{\text{SM}}$. *Right panel:* Comparison between the allowed region of parameter space in our model with the choice $\lambda_{H\phi} = \lambda_{H'\phi}$ (blue region) and the allowed region of parameter space in the corresponding 2HDM (yellow region).

shape of the allowed region in parameter space does not depend on them and coincides with that of the blue region. As suggested by (64) and (65), the latter depends on μ_3 , v_ϕ and β . To showcase the dependence on the first two parameters, in the left panel of Fig. 10 we report the parameter space for a different choice of μ_3 and v_ϕ . In passing, we note that the above remarks make our results slightly more general and apply, to some extent, to the case of 2HDMs. A comparison between the parameter space in Fig. 9 and the one obtained when the scalar singlet is removed (that is, keeping only the constraints on λ_2, λ_{34} and putting all the parameters related to the scalar singlet to zero) is shown in Fig. 10

We performed a numerical investigation of the parameter space with parameters fixed as in the right panel of Fig. 9. As a general property, it is easily understood that at fixed λ_1 the Landau pole increases and the instability scale decreases as α increases, while at fixed α the Landau pole decreases and the instability scale increases (or disappear for sufficiently low Landau poles) as λ_1 increases. We found that the competition between these two behaviours is such that on the lower boundary of the allowed region the Landau pole has only very mild variations. This curve of “constant Landau pole”, defined by the equation $\lambda_3 + 2\sqrt{\lambda_1\lambda_2} = 0$ (we note here that it also approximately corresponds to $\lambda_2 = 0$ for $\alpha \lesssim 0.3$), maximizes the Landau pole, and represents the locus of parameter space where the largest hierarchy between the (in)stability scale and the scale at which perturbation theory becomes unreliable is realized. Combining these two observations, we can conclude that, as the tuned and aligned scenario (red point in Fig. 9) is itself in the vicinity of the lower boundary, the Landau pole cannot be lifted significantly with respect to that case.

In passing, we also show in Fig. 11 the curves of constant λ_2 . These curves give us a more comprehensive understanding of the strong sensitivity to the detuning of λ_1 as a result of their focusing in the small α regime. The smaller the value of α , the smaller the distance between the different curves. For $\alpha = \beta$, the relative distance between the point where $\lambda_2 = 0$ and

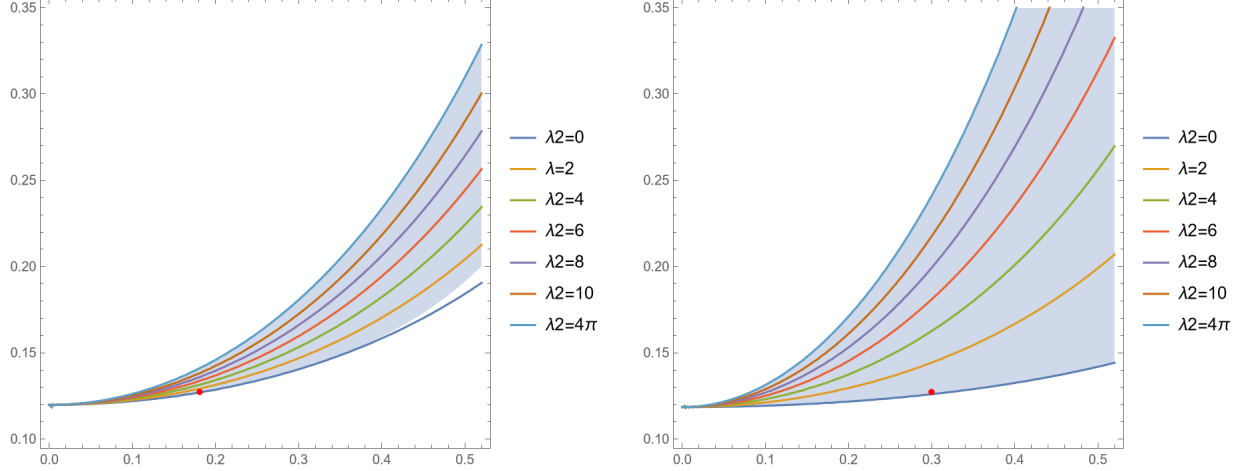


Figure 11: *Left panel:* Two dimensional section of the parameter space. The parameters have been chosen in the same way as in the middle panel of Fig. 9. The curves are the curves of constant λ_2 . *Right panel:* Same plot as in the left panel for a different choice of β , namely $\beta = 0.3$

the point where $\lambda_2 = 4\pi$ is $(\lambda_1^{\lambda_2=4\pi} - \lambda_1^{\lambda_2=0}) / \lambda_1^{\lambda_2=0} = 4\pi \sin^4 \beta / (\lambda_{\text{SM}} \cos 2\beta) \simeq 0.11$. This relative difference only depends on the angle β , and thus applies also to the corresponding 2HDM. This can be readily seen in the right panel of Fig. 10, where the vertical extension of the allowed region for $\alpha = \beta$ is the same as in our model. As the distance goes like $\sin^4 \beta / \cos 2\beta$, it grows for larger values of β , where the sensitivity to detuning becomes smaller and smaller. This can be seen, for instance, in the right panel of Fig. 11. The relative distance in the general, $\alpha \neq \beta$, case is

$$\delta\lambda \equiv \frac{\lambda_1^{\lambda_2=4\pi} - \lambda_1^{\lambda_2=0}}{\lambda_1^{\lambda_2=0}} = \frac{16\pi v^2 \sin^2 \alpha \sin^2 \beta}{\cos 2\alpha \left(4\lambda_{\text{SM}} v^2 - \frac{\mu_3 v_\phi}{\sin \beta \cos \beta} \right) + 2\mu_3 v_\phi \cot 2\beta}. \quad (67)$$

The peculiar shape of the allowed region of parameter space shown in Fig. 9 is easily understood with the above equation.

We report in Table 5 the results obtained for some points on the $\lambda_3 + 2\sqrt{\lambda_1 \lambda_2} = 0$ curve. The singularity in the running is always found around $\mu_L \sim 1.57 \times 10^9$ GeV. A peculiar feature that can be observed concerns the (in)stability scale. Moving from left to right in the (α, λ_1) parameter space, the flow of $\lambda_1(\mu)$ is always positive (that is, for all values of μ up to the perturbative scale) for $\alpha < \beta$. At some point, while α is still $\alpha < \beta$, the running coupling $\lambda_1(\mu)$ starts to develop an instability scale, that is, a scale where it crosses zero. The point $(\beta, \lambda_{\text{SM}})$ is very close from the “constant Landau pole” boundary, and is in fact found to have this kind of behaviour. This feature eventually disappears for larger values of α , where $\lambda_1(\mu)$ is again positive throughout its whole running. The results collected in Table 5 also seem to indicate that, when it exists, the instability scale is a convex function of α .

This leads us to the inevitable conclusion that if our model is to explain the muon $g - 2$ experimental anomaly, and possibly also the W mass one, it must necessarily be accompanied by new physics that must show up no further than $\mu \sim 10^9$ GeV. A more refined analysis

Benchmark points in Fig. 9 (<i>right</i>)									
α	λ_1	λ_2	λ_{34}	$\lambda_{H\phi}$	m_{h_2} (GeV)	m_s (GeV)	LP ($\times 10^9$ GeV)	VSB ($\times 10^7$ GeV)	Pert ($\times 10^8$ GeV)
0.14	0.1241	~ 0	0.3621	0.0526	219.83	178.08	1.57	—	7.22
β	0.1271	~ 0	0.2629	0.0590	220.28	178.50	1.57	9.60	7.30
0.22	0.1306	~ 0	0.1671	0.0651	220.87	178.95	1.58	6.52	7.35
0.26	0.1351	~ 0	0.0672	0.0714	221.65	179.46	1.57	12.3	7.36
0.3	0.1405	0.0022	-0.0352	0.0777	222.64	180.03	1.57	73.7	7.31
0.34	0.1468	0.0035	-0.1401	0.0840	223.84	180.63	1.55	—	7.25
0.38	0.1544	0.0375	-0.2528	0.0905	225.52	181.41	1.48	—	6.76

Table 5: Landau pole, stability scale and perturbativity scale for the benchmark points in the right plot of Fig. 9. We chose $\sin \beta = 0.18$.

might lead to a more precise definition of the upper bound for the appearance of new physics, but is not expected to change it much.

6 Conclusions

We presented in this work new results on the RG flow towards high energies in lepton portal models where both the muon $g-2$ and the W boson experimental anomalies can be explained simultaneously. We found that the choice of parameters favored by the SM anomalies results in unacceptably low Landau pole scales at $\mu_L \sim 10 - 100$ TeV in the alignment limit for the quartic couplings in the extended Higgs sector. Making a thorough analysis in the Higgs sector with more general relations, we showed that the Landau pole scale μ_L can be lifted up to $\mu_L \gtrsim 10^9$ GeV, and identified a preferred region of parameter space that maximizes μ_L while still fitting the experimental anomalies. Such a region of parameter space can potentially ameliorate the stability of the scalar potential. We also showed that, in the cases considered, stringent constraints arise from the Higgs data for scalar couplings and parameters in general scenarios that realize a detuning of the Higgs quartic couplings and/or a misalignment of the two Higgs doublets.

As a by-product of our analysis, we learned that if our model is to explain the experimental anomalies, it must be accompanied by new physics that must necessarily appear at scales $\mu \lesssim 10^9$ GeV. Concerning stability, this means that, if it couples strongly enough to the Higgs doublet H , such new physics could potentially deviate the RG flow of $\lambda_1(\mu)$ before the latter becomes negative. A final verdict on the existence of a vacuum deeper than the EW one in our model can then only be obtained through the knowledge of its $\mu \sim 10^9$ GeV completion. Our results on the flow of $\lambda_1(\mu)$ should thus be taken as indicating regions of parameter space where the quartic coupling can be lifted to positive values with no need for additional UV physics to do it. A complete study of stability within our model should also contemplate other possibilities, such as the possibility that the running coupling is lifted by additional states, or that the EW vacuum is a metastable one with a sufficiently long

lifetime. In both cases, knowledge of the UV physics completing the model is necessary to draw any conclusion.

Acknowledgments

The work is supported in part by Basic Science Research Program through the National Research Foundation of Korea (NRF) funded by the Ministry of Education, Science and Technology (NRF-2022R1A2C2003567) and JSPS KAKENHI Grant Number JP24K17040 (KY).

Appendices

A Mass matrices

We present the effective mass matrices for scalars, gauge bosons and fermions in our model.

A.1 Scalar masses

The (h_1, h_2, s) background of (19)-(21) is unfit to the extraction of Renormalization Group Equations, as both the operators $|H|^2|H'|^2$ and $|H^\dagger H'|^2$ reduce to $h_1^2 h_2^2$ in it, and, when applying the background field method, there would be no way to differentiate the two. For the determination of mass matrices and RGEs, it is convenient to consider, for the two Higgs doublets, the slightly more general background configuration

$$H = \frac{1}{\sqrt{2}} \begin{pmatrix} 0 \\ h_1 \end{pmatrix}, \quad H' = \frac{1}{\sqrt{2}} \begin{pmatrix} h_3 \\ h_2 \end{pmatrix}. \quad (\text{A.1})$$

On this background, in fact, $|H|^2|H'|^2 = h_1^2(h_2^2 + h_3^2)/4$, while $|H^\dagger H'| = h_1^2 h_2^2/4$. Contributions that renormalize the coupling λ_3 can then be distinguished from contributions that renormalize the coupling λ_4 . At the end of the calculation, that is after Renormalization Group Equations have been extracted, one is free to consider the simpler background configuration with $h_3 = 0$.

Expanding the potential (4) around the (h_1, h_2, h_3, s) background with parametrization

$$H = \frac{1}{\sqrt{2}} \begin{pmatrix} \phi_1 + i\phi_2 \\ h_1 + \rho_1 + i\eta_1 \end{pmatrix}, \quad (\text{A.2})$$

$$H' = \frac{1}{\sqrt{2}} \begin{pmatrix} h_3 + \phi_3 + i\phi_4 \\ h_2 + \rho_2 + i\eta_2 \end{pmatrix}, \quad (\text{A.3})$$

$$\phi = \frac{1}{\sqrt{2}}(s + \rho_3 + i\eta_3). \quad (\text{A.4})$$

we find a 10×10 mass matrix. Arranging its entries in the order $(\rho_1, \rho_2, \rho_3, \eta_1, \eta_2, \eta_3, \phi_1, \phi_2, \phi_3, \phi_4)$, it reads

$$\mathcal{M}_S^2 = \begin{pmatrix} a & b & d & 0 & 0 & 0 & \alpha & 0 & \beta & 0 \\ b & c & e & 0 & 0 & 0 & \gamma & 0 & \delta & 0 \\ d & e & f & 0 & 0 & 0 & \eta & 0 & \theta & 0 \\ 0 & 0 & 0 & a' & b' & d' & 0 & \zeta & 0 & 0 \\ 0 & 0 & 0 & b' & c' & e' & 0 & \xi & 0 & 0 \\ 0 & 0 & 0 & d' & e' & f' & 0 & \psi & 0 & 0 \\ \alpha & \gamma & \eta & 0 & 0 & 0 & A & 0 & C & 0 \\ 0 & 0 & 0 & \zeta & \xi & \psi & 0 & B & 0 & E \\ \beta & \delta & \theta & 0 & 0 & 0 & C & 0 & D & 0 \\ 0 & 0 & 0 & 0 & 0 & 0 & 0 & E & 0 & F \end{pmatrix}, \quad (\text{A.5})$$

with

$$a = \mu_1^2 + 3\lambda_1 h_1^2 + \frac{\lambda_3}{2}(h_2^2 + h_3^2) + \frac{\lambda_4}{2}h_2^2 + \frac{\lambda_{H\phi}}{2}s^2, \quad (\text{A.6})$$

$$b = (\lambda_3 + \lambda_4)h_1 h_2 - \frac{\mu_3}{\sqrt{2}}s, \quad (\text{A.7})$$

$$c = \mu_2^2 + 3\lambda_2 h_2^2 + \lambda_2 h_3^2 + \frac{\lambda_3 + \lambda_4}{2}h_1^2 + \frac{\lambda_{H'\phi}}{2}s^2, \quad (\text{A.8})$$

$$d = \lambda_{H\phi}h_1 s - \frac{\mu_3}{\sqrt{2}}h_2, \quad (\text{A.9})$$

$$e = \lambda_{H'\phi}h_2 s - \frac{\mu_3}{\sqrt{2}}h_1, \quad (\text{A.10})$$

$$f = \mu_\phi^2 + 3\lambda_\phi s^2 + \frac{\lambda_{H\phi}}{2}h_1^2 + \frac{\lambda_{H'\phi}}{2}(h_2^2 + h_3^2), \quad (\text{A.11})$$

$$a' = \mu_1^2 + \lambda_1 h_1^2 + \frac{\lambda_3}{2} (h_2^2 + h_3^2) + \frac{\lambda_4}{2} h_2^2 + \frac{\lambda_{H\phi}}{2} s^2, \quad (\text{A.12})$$

$$b' = -\frac{\mu_3}{\sqrt{2}} s, \quad (\text{A.13})$$

$$c' = \mu_2^2 + \lambda_2 (h_2^2 + h_3^2) + \frac{\lambda_3 + \lambda_4}{2} h_1^2 + \frac{\lambda_{H'\phi}}{2} s^2, \quad (\text{A.14})$$

$$d' = -\frac{\mu_3}{\sqrt{2}} h_2, \quad (\text{A.15})$$

$$e' = \frac{\mu_3}{\sqrt{2}} h_1, \quad (\text{A.16})$$

$$f' = \mu_\phi^2 + \lambda_\phi s^2 + \frac{\lambda_{H\phi}}{2} h_1^2 + \frac{\lambda_{H'\phi}}{2} (h_2^2 + h_3^2), \quad (\text{A.17})$$

$$A = \mu_1^2 + \lambda_1 h_1^2 + \frac{\lambda_3}{2} (h_2^2 + h_3^2) + \frac{\lambda_4}{2} h_3^2 + \frac{\lambda_{H\phi}}{2} s^2 = B, \quad (\text{A.18})$$

$$C = \frac{\lambda_4}{2} h_1 h_2 - \frac{\mu_3}{\sqrt{2}} s = E, \quad (\text{A.19})$$

$$D = \mu_2^2 + \lambda_2 h_2^2 + 3\lambda_2 h_3^2 + \frac{\lambda_3}{2} h_1^2 + \frac{\lambda_{H'\phi}}{2} s^2, \quad (\text{A.20})$$

$$F = \mu_2^2 + \lambda_2 (h_2^2 + h_3^2) + \frac{\lambda_3}{2} h_1^2 + \frac{\lambda_{H'\phi}}{2} s^2, \quad (\text{A.21})$$

$$\alpha = \frac{\lambda_4}{2} h_2 h_3, \quad \beta = \lambda_3 h_1 h_3, \quad \gamma = \frac{\lambda_4}{2} h_1 h_3, \quad (\text{A.22})$$

$$\delta = 2\lambda_2 h_2 h_3, \quad \eta = -\frac{\mu_3}{\sqrt{2}} h_3, \quad \theta = \lambda_{H'\phi} h_3 s, \quad (\text{A.23})$$

$$\zeta = \frac{\lambda_4}{2} h_2 h_3, \quad \xi = -\frac{\lambda_4}{2} h_1 h_3, \quad \psi = -\frac{\mu_3}{\sqrt{2}} h_3. \quad (\text{A.24})$$

When $h_3 = 0$, the Higgs-like, Goldstone-like and charged scalars decouple, and three different mass matrices can be individuated for each of them, as usual. In the text, we denote with \mathcal{M}_H^2 the upper 3×3 matrix of the Higgs-like excitations.

A.2 Gauge masses

Expanding the covariant derivatives around the background, we we find the following 5×5 mass matrix in the $(W_\mu^1, W_\mu^2, B_\mu, W_\mu^3, Z'_\mu)$ (in the unitary gauge)

$$\mathcal{M}_V^2 = \begin{pmatrix} \frac{g^2}{4} h_{123}^2 & 0 & \frac{gg_Y}{2} h_2 h_3 & 0 & 2gg_{Z'} h_2 h_3 \\ 0 & \frac{g^2}{4} h_{123}^2 & 0 & 0 & 0 \\ \frac{gg_Y}{2} h_2 h_3 & 0 & \frac{g_Y^2}{4} h_{123}^2 & \frac{gg_Y}{4} (h_3^2 - h^2) & g_Y g_{Z'} (h_2^2 + h_3^2) \\ 0 & 0 & \frac{gg_Y}{4} (h_3^2 - h^2) & \frac{g^2}{4} h_{123}^2 & gg_{Z'} (h_3^2 - h_2^2) \\ 2gg_{Z'} h_2 h_3 & 0 & g_Y g_{Z'} (h_2^2 + h_3^2) & gg_{Z'} (h_3^2 - h_2^2) & 4g_{Z'}^2 (s^2 + h_2^2 + h_3^2) \end{pmatrix} \quad (\text{A.25})$$

with $h^2 \equiv h_1^2 + h_2^2$, $h_{123}^2 \equiv h_1^2 + h_2^2 + h_3^2$. It is immediate to verify that, when $h_3 = 0$, W^1 and W^2 decouple, giving rise to the usual W mass, while the other three components form a 3×3 mass matrix that we refer to with the symbol \mathcal{M}_Z^2 in the text.

A.3 Fermion masses

When $h_3 \neq 0$, a fermion mass matrix for the muon, muon neutrino and the VLL can be written. The right-handed neutrino serves only to write a 3×3 matrix and can be safely ignored later, especially when we deal with the background considered in the text, where $h_3 = 0$.

We consider the mass terms for the lepton doublet and the vector-like lepton as

$$\begin{aligned} \mathcal{L}_{L,\text{mass}} &= -M_E \bar{E} E - m_0 \bar{e} e - (m_R \bar{E}_L e_R + m_L \bar{e}_L E_R + m_\nu \bar{\nu}_L E_R + \text{h.c.}) \\ &= -(\bar{\nu}_L, \bar{e}_L, \bar{E}_L) \mathcal{M}_L \begin{pmatrix} \nu_R \\ e_R \\ E_R \end{pmatrix} + \text{h.c.} \end{aligned} \quad (\text{A.26})$$

where

$$\mathcal{M}_L = \begin{pmatrix} 0 & 0 & m_\nu \\ 0 & m_0 & m_L \\ 0 & m_R & M_E \end{pmatrix}. \quad (\text{A.27})$$

Here, m_0 is the bare lepton mass $m_0 = \frac{1}{\sqrt{2}} y_l h_1$, m_R and m_L are the mixing masses given by $m_R = \frac{1}{\sqrt{2}} \lambda_{ES}$ and $m_L = \frac{1}{\sqrt{2}} y_E h_2$, respectively, and $m_\nu = \frac{1}{\sqrt{2}} y_E h_3$. The squared mass matrix is thus

$$\mathcal{M}_f^2 \equiv \mathcal{M}_L^\dagger \mathcal{M}_L = \begin{pmatrix} 0 & 0 & 0 \\ 0 & m_0^2 + m_R^2 & m_0 m_L + m_R M_E \\ 0 & m_0 m_L + m_R M_E & m_\nu^2 + m_L^2 + M_E^2 \end{pmatrix}. \quad (\text{A.28})$$

Finally, the top quark mass is $m_t = \frac{y_t}{\sqrt{2}} h_1$.

B Renormalization Group Equations

We present the RG equations for the parameters in the scalar potential, gauge and Yukawa couplings in the model.

B.1 Extraction of the scalar RGEs from the potential

Inserting the explicit expressions (22) and (23) in (25) we obtain the following system of equations (k is the running scale, the symbols β_{λ_i} and γ_{μ_i} indicate $k \frac{d}{dk} \lambda_i$ and $k \frac{d}{dk} \mu_i$, re-

spectively, γ_i are the anomalous dimensions and α_i are the coefficients of the quadratically UV-sensitive terms defined in (24)):

$$\mu_1^2 \gamma_{\mu_1^2} - 2\gamma_1 \mu_1^2 = -2\alpha_1 k^2 + \frac{6\lambda_1 \mu_1^2 + 2(\lambda_3 + \lambda_4) \mu_2^2 + \lambda_{H\phi} \mu_\phi^2 + \mu_3^2}{8\pi^2}, \quad (\text{B.1})$$

$$\mu_2^2 \gamma_{\mu_2^2} - 2\gamma_2 \mu_2^2 = -2\alpha_2 k^2 + \frac{6\lambda_2 \mu_2^2 + 2\lambda_3 \mu_1^2 + \lambda_4 \mu_1^2 + \lambda_{H'\phi} \mu_\phi^2 + \mu_3^2 - 2y_E^2 M_E^2}{8\pi^2}, \quad (\text{B.2})$$

$$\mu_\phi^2 \gamma_{\mu_\phi^2} - 2\gamma_\phi \mu_\phi^2 = -2\alpha_3 k^2 + \frac{4\lambda_\phi \mu_\phi^2 + 2\lambda_{H\phi} \mu_1^2 + 2\lambda_{H'\phi} \mu_2^2 + 2\mu_3^2 - 2\lambda_E^2 M_E^2}{8\pi^2}, \quad (\text{B.3})$$

$$\beta_{\lambda_1} - 4\gamma_1 \lambda_1 = \frac{9g^4 + 6g^2 g_Y^2 + 3g_Y^4}{128\pi^2} + \frac{3\lambda_1^2}{2\pi^2} + \frac{2\lambda_3(\lambda_3 + \lambda_4) + \lambda_4^2}{16\pi^2} + \frac{\lambda_{H\phi}^2}{16\pi^2} - \frac{3y_t^4 + y_l^4}{8\pi^2}, \quad (\text{B.4})$$

$$\begin{aligned} \beta_{\lambda_2} - 4\gamma_2 \lambda_2 &= \frac{9g^4 + 6g^2 g_Y^2 + 3g_Y^4}{128\pi^2} + \frac{3g_{Z'}^2 (g^2 + g_Y^2) + 24g_{Z'}^4}{4\pi^2} + \frac{3\lambda_2^2}{2\pi^2} \\ &+ \frac{2\lambda_3(\lambda_3 + \lambda_4) + \lambda_4^2}{16\pi^2} + \frac{\lambda_{H'\phi}^2}{16\pi^2} - \frac{y_E^4}{8\pi^2}, \end{aligned} \quad (\text{B.5})$$

$$\beta_{\lambda_\phi} - 4\gamma_\phi \lambda_\phi = \frac{6g_{Z'}^4}{\pi^2} + \frac{5\lambda_\phi^2}{4\pi^2} + \frac{\lambda_{H\phi}^2}{8\pi^2} + \frac{\lambda_{H'\phi}^2}{8\pi^2} - \frac{\lambda_E^4}{8\pi^2}, \quad (\text{B.6})$$

$$\beta_{\lambda_3} - 2(\gamma_1 + \gamma_2) \lambda_3 = \frac{9g^4 - 6g^2 g_Y^2 + 3g_Y^4}{64\pi^2} + \frac{(\lambda_1 + \lambda_2)(6\lambda_3 + 2\lambda_4) + 2\lambda_3^2 + \lambda_4^2}{8\pi^2} + \frac{\lambda_{H\phi} \lambda_{H'\phi}}{8\pi^2}, \quad (\text{B.7})$$

$$\beta_{\lambda_4} - 2(\gamma_1 + \gamma_2) \lambda_4 = \frac{3g^2 g_Y^2}{16\pi^2} + \frac{\lambda_4(\lambda_1 + \lambda_2 + 2\lambda_3 + \lambda_4)}{4\pi^2} - \frac{y_E^2 y_l^2}{4\pi^2}, \quad (\text{B.8})$$

$$\beta_{\lambda_{H\phi}} - 2(\gamma_1 + \gamma_\phi) \lambda_{H\phi} = \frac{2\lambda_{H\phi}^2 + 6\lambda_1 \lambda_{H\phi} + 4\lambda_\phi \lambda_{H\phi} + 2\lambda_3 \lambda_{H'\phi} + \lambda_4 \lambda_{H'\phi}}{8\pi^2} - \frac{\lambda_E^2 y_l^2}{4\pi^2}, \quad (\text{B.9})$$

$$\beta_{\lambda_{H'\phi}} - 2(\gamma_2 + \gamma_\phi) \lambda_{H'\phi} = \frac{12g_{Z'}^4}{\pi^2} + \frac{2\lambda_{H'\phi}^2 + 6\lambda_2 \lambda_{H'\phi} + 4\lambda_\phi \lambda_{H'\phi} + 2\lambda_3 \lambda_{H\phi} + \lambda_4 \lambda_{H\phi}}{8\pi^2}, \quad (\text{B.10})$$

$$\beta_{\mu_3} - (\gamma_1 + \gamma_2 + \gamma_\phi) \mu_3 = \frac{\lambda_3 + 2\lambda_4 + \lambda_{H\phi} + \lambda_{H'\phi}}{8\pi^2} \mu_3 + \frac{y_E \lambda_E y_l M_E}{4\pi^2}. \quad (\text{B.11})$$

The equations above are Wilsonian RG equations in the UV regime of the flow defined as $k^2 \gg m_i(k)^2$, with $m_i(k)$ the physical running masses. Subtracting the terms proportional to k^2 from the first three equations, that corresponds to performing a fine-tuning in perturbation theory and putting the system close to the critical surface of the Gaussian fixed point in the broader RG context [33], the usual perturbative RGEs are found.

The anomalous dimensions can be calculated from the two-point functions of h_1 , h_2 and s as

$$\gamma_i = -\frac{1}{2} \Lambda \frac{\partial}{\partial \Lambda} \left(\frac{\partial}{\partial p^2} \Sigma(p^2) \right)_{p^2=m_i^2}. \quad (\text{B.12})$$

As it is well-known, the only diagrams that contribute at the one-loop level are fermionic sunset diagrams and mixed gauge-Goldstone sunset diagrams (pure gauge diagrams can also give p^2 contributions that are however suppressed by powers of Λ , so they do not contribute

to the beta function). The results for anomalous dimensions are

$$\begin{cases} \gamma_1 = -\frac{1}{16\pi^2} \left(\frac{3}{4} (3g^2 + g_Y^2) - 3y_t^2 - y_l^2 \right), \\ \gamma_2 = -\frac{1}{16\pi^2} \left(\frac{3}{4} (3g^2 + g_Y^2) + 12g_{Z'}^2 - y_E^2 \right), \\ \gamma_\phi = -\frac{1}{16\pi^2} \left(12g_{Z'}^2 - \lambda_E^2 \right). \end{cases} \quad (\text{B.13})$$

B.2 Gauge RGEs

The general equation for the non-abelian gauge RGEs is

$$\beta_g = -\frac{g^3}{16\pi^3} \left(\frac{11}{3} C_2(G) - \frac{4}{3} n_f C(r) - \frac{1}{3} n_s C(r) \right) \quad (\text{B.14})$$

where $C_2(G) = N$ and $C(r) = 1/2$ for $SU(N)$.

- For $SU(3)$ we have, as in the SM, $n_f = 6$, $n_s = 0$;
- For $SU(2)$ we have the same DOFs as in the SM plus the second Higgs doublet, so that $n_f = 6$ and $n_s = 2$.

For $U(1)$ groups we have in general

$$\beta_g = \frac{g^3}{12\pi^2} \left(\sum_i n_f^i (q_f^i)^2 + \frac{1}{4} n_s^i (q_s^i)^2 \right). \quad (\text{B.15})$$

where q^i are the charges under the gauge group.

The straightforward application of these equations to our model leads to the following RGEs for the gauge couplings

$$\begin{cases} \beta_{g_s} = -\frac{7}{16\pi^2} g_s^3, \\ \beta_g = -\frac{3}{16\pi^2} g^3, \\ \beta_{g_Y} = \frac{25}{48\pi^2} g_Y^3, \\ \beta_{g_{Z'}} = \frac{7}{12\pi^2} g_{Z'}^3 \end{cases} \quad (\text{B.16})$$

where g_s is the strong coupling, g the $SU(2)$ coupling, g_Y the hypercharge one and $g_{Z'}$ the $U(1)'$ one.

B.3 Fermion RGEs

The well-known RGE for the top Yukawa coupling is

$$\beta_{y_t} = \frac{y_t}{16\pi^2} \left(\frac{9}{2} y_t^2 - 8g_3^2 - \frac{9}{4} g^2 - \frac{17}{12} g'^2 \right). \quad (\text{B.17})$$

Calculating the relevant diagrams, we find for the two other Yukawa couplings the following set of RGEs

$$\begin{cases} \beta_{y_E} = \frac{y_E}{16\pi^2} \left(\frac{5}{2}y_E^2 + \frac{y_l^2}{2} - \frac{15}{4}g_Y^2 - \frac{9}{4}g^2 - 12g_{Z'}^2 \right) \\ \beta_{\lambda_E} = \frac{\lambda_E}{16\pi^2} \left(2\lambda_E^2 + y_l^2 - 6g_Y^2 - 12g_{Z'}^2 \right). \end{cases}$$

The last two equations needed to close the full set of RGEs are those for M_E and y_l . They are easily found and read

$$\begin{cases} \gamma_M = \frac{3g_Y^2 + 12g_{Z'}^2}{8\pi^2} \\ \beta_{y_l} = \frac{y_l}{16\pi^2} \left(\frac{y_E^2 + \lambda_E^2}{2} + 3y_t^2 + \frac{3}{2}y_l^2 - \frac{9}{4}g^2 - \frac{15}{4}g_Y^2 \right) \end{cases} \quad (\text{B.18})$$

where $\gamma_M = \frac{k}{M} \frac{\partial M}{\partial k}$.

References

- [1] J. Elias-Miro, J. R. Espinosa, G. F. Giudice, G. Isidori, A. Riotto and A. Strumia, *Higgs mass implications on the stability of the electroweak vacuum*, Phys. Lett. B **709** (2012), 222-228, [arXiv:1112.3022](#) [hep-ph]; G. Degrandi, S. Di Vita, J. Elias-Miro, J. R. Espinosa, G. F. Giudice, G. Isidori and A. Strumia, *Higgs mass and vacuum stability in the Standard Model at NNLO*, JHEP **08** (2012), 098, [arXiv:1205.6497](#) [hep-ph].
- [2] J. Elias-Miro, J. R. Espinosa, G. F. Giudice, H. M. Lee and A. Strumia, *Stabilization of the Electroweak Vacuum by a Scalar Threshold Effect*, JHEP **06** (2012), 031, [arXiv:1203.0237](#) [hep-ph].
- [3] V. Branchina and E. Messina, *Stability, Higgs Boson Mass and New Physics*, Phys. Rev. Lett. **111**, 241801 (2013), [arXiv:1307.5193](#) [hep-ph]; V. Branchina and E. Messina, *Stability and UV completion of the Standard Model*, EPL **117**, no.6, 61002 (2017), [arXiv:1507.08812](#) [hep-ph]; A. Andreassen, D. Farhi, W. Frost and M. D. Schwartz, *Precision decay rate calculations in quantum field theory*, Phys. Rev. D **95**, no.8, 085011 (2017), [arXiv:1604.06090](#) [hep-th].
- [4] G. W. Bennett *et al.* [Muon g-2], *Final Report of the Muon E821 Anomalous Magnetic Moment Measurement at BNL*, Phys. Rev. D **73** (2006), 072003, [arXiv:hep-ex/0602035](#) [hep-ex].
- [5] B. Abi *et al.* [Muon g-2], *Measurement of the Positive Muon Anomalous Magnetic Moment to 0.46 ppm*, Phys. Rev. Lett. **126** (2021) no.14, 141801, [arXiv:2104.03281](#) [hep-ex].
- [6] T. Aaltonen *et al.* [CDF], *High-precision measurement of the W boson mass with the CDF II detector*, Science **376** (2022) no.6589, 170-176

- [7] T. Aoyama, N. Asmussen, M. Benayoun, J. Bijnens, T. Blum, M. Bruno, I. Caprini, C. M. Carloni Calame, M. Cè and G. Colangelo, *et al.* Phys. Rept. **887** (2020), 1-166 doi:10.1016/j.physrep.2020.07.006 [[arXiv:2006.04822](#) [hep-ph]].
- [8] S. Borsanyi, Z. Fodor, J. N. Guenther, C. Hoelbling, S. D. Katz, L. Lellouch, T. Lippert, K. Miura, L. Parato and K. K. Szabo, *et al.* Nature **593** (2021) no.7857, 51-55 doi:10.1038/s41586-021-03418-1 [[arXiv:2002.12347](#) [hep-lat]].
- [9] A. Boccaletti, S. Borsanyi, M. Davier, Z. Fodor, F. Frech, A. Gerardin, D. Giusti, A. Y. Kotov, L. Lellouch and T. Lippert, *et al.* [[arXiv:2407.10913](#) [hep-lat]].
- [10] F. V. Ignatov *et al.* [CMD-3], Phys. Rev. Lett. **132** (2024) no.23, 231903 doi:10.1103/PhysRevLett.132.231903 [[arXiv:2309.12910](#) [hep-ex]].
- [11] H. M. Lee and K. Yamashita, *A model of vector-like leptons for the muon $g - 2$ and the W boson mass*, Eur. Phys. J. C **82** (2022) no.8, 661, [arXiv:2204.05024](#) [hep-ph].
- [12] G. Hiller, C. Hormigos-Feliu, D. F. Litim and T. Steudtner, *Anomalous magnetic moments from asymptotic safety*, Phys. Rev. D **102** (2020) no.7, 071901, [arXiv:1910.14062](#) [hep-ph].
- [13] G. Hiller, C. Hormigos-Feliu, D. F. Litim and T. Steudtner, *Model Building from Asymptotic Safety with Higgs and Flavor Portals*, Phys. Rev. D **102** (2020) no.9, 095023, [arXiv:2008.08606](#) [hep-ph].
- [14] H. M. Lee, *Exothermic dark matter for XENON1T excess*, JHEP **01** (2021), 019, [arXiv:2006.13183](#) [hep-ph].
- [15] H. M. Lee, J. Song and K. Yamashita, *Seesaw lepton masses and muon $g-2$ from heavy vector-like leptons*, J. Korean Phys. Soc. **79** (2021) no.12, 1121-1134, [arXiv:2110.09942](#) [hep-ph].
- [16] G. C. Branco, P. M. Ferreira, L. Lavoura, M. N. Rebelo, M. Sher and J. P. Silva, *Theory and phenomenology of two-Higgs-doublet models*, Phys. Rept. **516** (2012), 1-102, [arXiv:1106.0034](#) [hep-ph]].
- [17] L. Bian, H. M. Lee and C. B. Park, *B -meson anomalies and Higgs physics in flavored $U(1)'$ model*, Eur. Phys. J. C **78** (2018) no.4, 306, [arXiv:1711.08930](#) [hep-ph].
- [18] S. S. Kim, H. M. Lee, A. G. Menkara and K. Yamashita, *$SU(2)_D$ lepton portals for the muon $g-2$, W -boson mass, and dark matter*, Phys. Rev. D **106** (2022) no.1, 015008, [arXiv:2205.04016](#) [hep-ph].
- [19] J. Alwall, R. Frederix, S. Frixione, V. Hirschi, F. Maltoni, O. Mattelaer, H. S. Shao, T. Stelzer, P. Torrielli and M. Zaro, *The automated computation of tree-level and next-to-leading order differential cross sections, and their matching to parton shower simulations*, JHEP **07**, 079 (2014), [[arXiv:1405.0301](#) [hep-ph]].

- [20] A. Alloul, N. D. Christensen, C. Degrande, C. Duhr and B. Fuks, *FeynRules 2.0 - A complete toolbox for tree-level phenomenology*, Comput. Phys. Commun. **185**, 2250-2300 (2014), [arXiv:1310.1921](#) [hep-ph].
- [21] G. Aad *et al.* [ATLAS], *Search for high-mass dilepton resonances using 139 fb⁻¹ of pp collision data collected at $\sqrt{s} = 13$ TeV with the ATLAS detector*, Phys. Lett. B **796**, 68-87 (2019), [arXiv:1903.06248](#) [hep-ex].
- [22] [ATLAS], ATLAS-CONF-2022-066.
- [23] G. Aad *et al.* [ATLAS], *Search for direct production of electroweakinos in final states with one lepton, missing transverse momentum and a Higgs boson decaying into two b-jets in pp collisions at $\sqrt{s} = 13$ TeV with the ATLAS detector*, Eur. Phys. J. C **80**, no.8, 691 (2020), [arXiv:1909.09226](#) [hep-ex].
- [24] G. Aad *et al.* [ATLAS], *Search for heavy resonances decaying into a Z or W boson and a Higgs boson in final states with leptons and b-jets in 139 fb⁻¹ of pp collisions at $\sqrt{s} = 13$ TeV with the ATLAS detector*, JHEP **06**, 016 (2023), [arXiv:2207.00230](#) [hep-ex].
- [25] [ATLAS], *Summary of Diboson Resonance Searches at the ATLAS experiment using full run-2 data*, ATL-PHYS-PUB-2023-007.
- [26] K. Kannike, *Vacuum Stability Conditions From Copositivity Criteria*, Eur. Phys. J. C **72** (2012), 2093, [arXiv:1205.3781](#) [hep-ph].
- [27] P. M. Ferreira, R. Santos and A. Barroso, *Stability of the tree-level vacuum in two Higgs doublet models against charge or CP spontaneous violation*, Phys. Lett. B **603** (2004), 219-229 [erratum: Phys. Lett. B **629** (2005), 114-114], [arXiv:hep-ph/0406231](#) [hep-ph].
- [28] A. Barroso, P. M. Ferreira and R. Santos, *Charge and CP symmetry breaking in two Higgs doublet models*, Phys. Lett. B **632** (2006), 684-687, [arXiv:hep-ph/0507224](#) [hep-ph].
- [29] I. P. Ivanov, *Minkowski space structure of the Higgs potential in 2HDM*, Phys. Rev. D **75** (2007), 035001 [erratum: Phys. Rev. D **76** (2007), 039902], [arXiv:hep-ph/0609018](#) [hep-ph].
- [30] I. P. Ivanov, *Minkowski space structure of the Higgs potential in 2HDM. II. Minima, symmetries, and topology*, Phys. Rev. D **77** (2008), 015017, [arXiv:0710.3490](#) [hep-ph].
- [31] A. Barroso, P. M. Ferreira and R. Santos, *Neutral minima in two-Higgs doublet models*, Phys. Lett. B **652** (2007), 181-193, [arXiv:hep-ph/0702098](#) [hep-ph].
- [32] V. Branchina, F. Contino and P. M. Ferreira, *Electroweak vacuum lifetime in two Higgs doublet models*, JHEP **11** (2018), 107, [arXiv:1807.10802](#) [hep-ph].

- [33] C. Branchina, V. Branchina and F. Contino, *Physical tuning and naturalness*, Phys. Rev. D **107** (2023) no.9, 096012, [arXiv:2208.05431](#) [hep-ph].
- [34] M. x. Luo, H. w. Wang and Y. Xiao, Phys. Rev. D **67** (2003), 065019 doi:10.1103/PhysRevD.67.065019 [[arXiv:hep-ph/0211440](#) [hep-ph]].
- [35] A. Pilaftsis, *Symmetries for standard model alignment in multi-Higgs doublet models*, Phys. Rev. D **93** (2016) no.7, 075012, [arXiv:1602.02017](#) [hep-ph].